UNIVERSITÄT BREMEN

MASTER THESIS

Accretion tori around compact objects with quadrupole moment

Author:
Jan-Menno MEMMEN

Examiner:
PD. Dr. Volker PERLICK
Second Examiner:
Prof. Dr. Claus LÄMMERZAHL

Manufactured in

Center of Applied Space Technology and Microgravity

Submitted to

Fachbereich 1 - Physik/Elektrotechnik

September 10, 2020

Declaration of Authorship

I, Jan-Menno MEMMEN, declare that this thesis titled, "Accretion tori around compact objects with quadrupole moment" and the work presented in it are my own. I confirm that:

- This work was done wholly or mainly while in candidature for a research degree at this University.

- Where any part of this thesis has previously been submitted for a degree or any other qualification at this University or any other institution, this has been clearly stated.

- Where I have consulted the published work of others, this is always clearly attributed.

- Where I have quoted from the work of others, the source is always given. With the exception of such quotations, this thesis is entirely my own work.

- I have acknowledged all main sources of help.

- Where the thesis is based on work done by myself jointly with others, I have made clear exactly what was done by others and what I have contributed myself.

Signed:

_____

Date:

_____

"Physics is about questioning, studying, probing nature. You probe, and, if you're lucky, you get strange clues."

Lene Hau

Contents

Chapter 1

Introduction

When a black hole is accreting mass at a low rate (below the Eddington limit), geometrically thick accretion discs are established, forming a torus. The behavior of perfect fluids in an equilibrium around a compact object is used as initial condition for simulations of accretion, and are of astrophysical importance.
As modern space technology is becoming more and more precise, allowing for more accurate astronomical observations, deformations of the source of gravity is becoming more important as well. Theoretically, this is expressed by the inclusion of higher-order multipole moments, the simplest of which is the quadrupole moment.

In this thesis, geometrically thick tori orbiting around compact objects with quadrupole moment are subject of study.

Firstly, the theoretical background is discussed.
This includes some background on the fundamentals of general relativity, the underlying theory on gravity, linking the curvature of spacetime to the local energy-matter distribution. After this, a short summary of perfect fluids in general relativity is given, as they are the main component of geometrically thick tori. This section is followed by a discussion on the spacetimes describing compact objects:

- the *Schwarzschild* metric, the simplest solution to Einsteins vacuum field equation, only possessing a monopole moment;

- the *q-metric*, the simplest solution of the vacuum field equations with multipole moments up to the quadrupole moment;

- the *Erez-Rosen* metric, the first exact solution of the vacuum Einstein equations describing a quadrupolar object.

This section also includes the properties of these compact objects (e.g., the metric), as well as the properties of light and particles orbiting such objects.
Following this section, there is a discussion on the theory behind geometrically thick tori. In this regard, the von-Zeipel cylinders and the specific angular momentum are of impoirtance, as they form the basis for the computation of the *effective potential*, which serves as the main quantity for analysing the properties and behavior of the tori.
There are limits on the specific angular momentum of the tori, and the theory and approach of calculating these limits close off the chapter on theory.

In the next chapter, geometrically thick tori orbiting a Schwarzschild black hole is studied. In particular, the von-Zeipel cylinders and the effective potential are calculated, and the effect of the specific angular momentum and its limits are discussed. The Schwarzschild tori serve as the object of comparison, as it does not retain any multipole moment higher than the monopole moment.

Next, there is a chapter on the study on geometrically thick tori orbiting a compact object described by the q-metric. Again, the von-Zeipel cylinders and the effective potential are calculated, and the impact of the quadrupole parameter on the behavior and properties of the tori is investigated. As the q-metric is the simplest exact solution to the vacuum field equations, most quantities are analytically calculable.

Afterwards, geometrically thick tori orbiting around an quadrupolar object described by the Erez-Rosen metric is discussed. This includes a study of the behavior and properties of the von-Zeipel cylinders and effective potential is conducted. As the Erez-Rosen metric is analytically cumbersome, the limits of the specific angular momentum are computed mostly numerically.

The last chapter is dedicated to comparing the effect of the quadrupole on the geometrical properties and behavior of geometrically thick tori for different spacetimes with quadrupole moment. In particular, the qualitative and quantitative differences of the influence of the quadrupole moment between tori in q-metric and Erez-Rosen spacetime is studied.

Chapter 2

Theory and Context

In this chapter, the theoretical foundation for the understanding of the motion of perfect fluids around massive object is created.

After a short introduction to the basic fundamentals of general relativity and conventions used in this thesis, the properties of perfect fluids are discussed.

As this thesis focuses on perfect fluids in motion around objects with quadrupole moment, three different spacetimes are discussed:

The *Schwarzschild* spacetime, which is the simplest solution to Einsteins field equations and will be used as a reference, as it only possesses a monopole moment;

The *Q metric*, an exact solution to the field equations which describes the exterior field of a naked singularity with quadrupole moment, and is generally considered to be the simplest spacetime that possesses a quadrupole moment;

And lastly, the *Erez-Rosen* spacetime, which is an exact solution of the vacuum Einstein equations describing a quadrupole body.

Following this section, the theoretical basis and underlying equations for the calculations and behavior of geometrically thick accretion tori are discussed, in particular the von-Zeipel cylinders, specific angular momentum and effective potential.

In the last section, the limits for the specific angular momentum where the equipotential surfaces of the tori are closed, are detailed. In this context, the approach of calculating the Keplerian specific angular momentum and marginally bound - and stable circular orbits are covered.

2.1 Fundamentals

In the context of general relativity, the metric is a second-degree covariant, symmetric, non-degenerate tensor on a four-dimensional differentiable manifold, which represents the spacetime mathematically.

Regarding this thesis, the metric is expressed by g with the convention of signature as (- + + +). Additionally, all Greek indices run from 0 to 3 and Einstein's summation convention is complied. Furthermore, geometrized units ($c = G = 1$) are adopted.

When discussing general relativity, geodesics are of particular importance. In the context of this thesis, geodesics are the shortest paths between two points in curved spacetime. Geodesics can be calculated by the geodesic equation [1, 2]

$$\frac{\mathrm{d}^2 x^\alpha}{\mathrm{d}s^2} + \Gamma^\alpha_{\mu\nu} \frac{\mathrm{d}x^\mu}{\mathrm{d}s} \frac{\mathrm{d}x^\nu}{\mathrm{d}s} = 0 \tag{2.1}$$

with s being a scalar parameter of motion and $\Gamma^\alpha_{\mu\nu}$ the coefficients of the Levi-Civita connection (also called Christoffel symbols). [3] The Levi-Civita connection is connected to the metric as

$$\Gamma^\alpha_{\mu\nu} = \frac{1}{2} g^{\alpha\beta} \left(\partial_\nu g_{\beta\mu} + \partial_\mu g_{\beta\nu} - \partial_\beta g_{\mu\nu} \right) \tag{2.2}$$

Lightlike geodesics ($g_{\mu\nu}\dot{x}^\mu\dot{x}^\nu = 0$) describe the motion of light and gives insight on the behavior of photons around compact objects. Timelike geodesics ($g_{\mu\nu}\dot{x}^\mu\dot{x}^\nu < 0$) describe the motion of free falling test particles. This is especially important when talking about accretion tori, matter orbiting a compact object.

A measure of the curvature of the spacetime is the *curvature tensor*; using the Levi-Civita connection, the curvature tensor can be expressed as [3]

$$R^\alpha_{\mu\nu\gamma} = \partial_\nu\Gamma^\alpha_{\gamma\mu} - \partial_\gamma\Gamma^\alpha_{\nu\mu} + \Gamma^\alpha_{\nu\beta}\Gamma^\beta_{\gamma\mu} - \Gamma^\alpha_{\gamma\beta}\Gamma^\beta_{\nu\mu} \tag{2.3}$$

The Einstein field equations relate the curvature of spacetime with the local energy-matter distribution and can be expressed as [4]

$$R_{\mu\nu} - \frac{1}{2}Rg_{\mu\nu} + \Lambda g_{\mu\nu} = 8\pi T_{\mu\nu} \tag{2.4}$$

where Λ is the cosmological constant, $T_{\mu\nu}$ is the energy-stress tensor describing the energy-matter distribution, $R_{\mu\nu}$ the Ricci tensor and $R = g^{\mu\nu}R_{\mu\nu}$ the curvature scalar.
The Ricci tensor can be expressed via the curvature tensor as the contraction like $R_{\mu\nu} = R^\alpha_{\mu\alpha\nu}$.
In the context of this thesis, mostly the vacuum field equations are considered; without any energy-mass distribution, and vanishing cosmological constant, the Einstein field equations reduce to

$$R_{\mu\nu} = 0 \tag{2.5}$$

2.2   Perfect fluids

The theory on geometrically thick tori depends on the understanding of perfect fluids, thus the theoretical background is shortly discussed. [5]

Perfect fluids are fluids where viscous effects and heat fluxes are neglected.
Elementary for describing any kind of matter distribution is the energy-momentum tensor $T^{\mu\nu}$. It expresses the flux of the μ-momentum in ν-direction. μ and ν denote the components of the vector moving with the fluid.
The energy-momentum tensor for perfect fluids can be written as

$$T^{\mu\nu} = (\rho + \frac{p}{c^2})u^\mu u^\nu + pg^{\mu\nu}, \tag{2.6}$$

where ρ is the energy density of the fluid, p the pressure, u^μ the four-velocity and $g^{\mu\nu}$ the metric representation.
Properties of the energy-momentum tensor follow accordingly:

- T_{00} denotes the energy density

- T_{0i} denotes the energy flux

- T_{i0} denotes the momentum density

- T_{ij} denotes the momentum flux

- T_{ii} denotes the isotropic pressure

From the conservation of energy and momentum $\nabla_\mu T^{\mu\nu} = 0$, the relativistic Euler equation for perfect fluids can be written as [6]

$$\left(\rho + \frac{p}{c^2}\right) u^\mu \partial_\mu u^\nu + \partial_\alpha p \left(g^{\alpha\nu} + \frac{1}{c^2} u^\alpha u^\nu\right) = 0 \tag{2.7}$$

Relativistic Bernoulli theorem

When looking for quantities in stationary flow constant along the fluidlines, the *relativistic Bernoulli theorem* states that

$$\mathcal{B} = h u_\mu \xi^\mu = \text{const.} \tag{2.8}$$

where h is the relativistic specific enthalpy and $\mathcal{B}$ is Lie-dragged along the fluidlines; ξ^μ describes the Killing vector. [7]

2.3 Space-times

In this section, the general properties of the spacetimes, which are considered in the analysis, are given in more detail. Moreover, a short discussion is made on the properties of the time- and lightlike geodesics.

First, the most simple solution of the vacuum field equations, the Schwarzschild solution, is covered. It is spherically symmetric and consequently only possesses a mass monopole moment.

Next, the most simple solution of the vacuum field equations with a quadrupole moment, the so-called q-metric, is detailed.

Last, the Erez-Rosen solution is covered, which was the first quadrupole metric which reduces to the Schwarzschild case for vanishing quadrupole parameter.

2.3.1 Schwarzschild

The most general axisymmetric, static and asymptotically flat solution of the vacuum field equations in Eq. (2.5) is represented by the Weyl class of solutions, the simplest of which is the spherically symmetric Schwarzschild metric. It describes the gravitational field outside any spherical mass; the metric is given by

$$ds^2 = -\left(1 - \frac{r_s}{r}\right) dt^2 + \frac{1}{1 - \frac{r_s}{r}} dr^2 + r^2 (d\vartheta^2 + \sin^2 \vartheta d\varphi^2), \tag{2.9}$$

where $r_s = \frac{2GM}{c^2} = 2M$ is the *Schwarzschild radius*. [8]

The metric in Eq. (2.9) has two singularities at $r = 0$ and $r = r_s$. By calculating curvature scalars (e.g., $R^{\alpha\beta\gamma\delta} R_{\alpha\beta\gamma\delta}$, see Eq. (2.3)), it is possible to see that there is a true curvature singularity at $r = 0$. The singularity at $r = r_s$ is an artifact of the chosen coordinates and can be removed by proper coordinate transformation (e.g., Eddington-Finkelstein coordinates, mapping outgoing radial lightlike geodesics onto straight lines).

Any object whose outer radius decreases below $r = 2M$ (e.g., the core of a star collapsing in a supernova [9]) must decrease to $r = 0$, forming a black hole. If located at $r < 2M$, nothing in (sub)luminal motion can escape the black hole. [10]

Lightlike and timelike circular geodesics in the equatorial plane

In the following section, lightlike and timelike circular geodesics in the equatorial plane are subject to study. Using the approach in terms of the Lagrangian $\mathcal{L} = g_{\mu\nu}\dot{x}^{\mu}\dot{x}^{\nu}$, the Euler-Lagrange equation for r can be expressed as:

$$\frac{dr}{d\tau} = \left[E^2 - \left(1 - \frac{2M}{r}\right)\left(\varepsilon + \frac{l^2}{r^2}\right)\right] =: \left[E^2 - V_{\text{eff}}\right], \tag{2.10}$$

where ε characterizes the type of geodesic. The specific energy E and the specific angular momentum of the test particle l are the constants of motion, and τ is the affine parameter.
The effective potential V_{eff} is important for the study of radial motion. In particular, circular motion with $\dot{r} \overset{!}{=} 0$ is equivalent to a test particle moving in the effective potential: [9]

$$V_{\text{eff}} = \left(1 - \frac{2M}{r}\right)\left(\frac{l^2}{r^2} + \varepsilon\right) \tag{2.11}$$

where $\varepsilon = 0$ for lightlike geodesics and $\varepsilon = 1$ for timelike geodesics.

The angular momentum of a test particle moving in timelike circular motion around the central object can be obtained when observing the extrema of the effective potential ($\partial_r V_{\text{eff}} \overset{!}{=} 0$):

$$\partial_r V_{\text{eff}} = \frac{2M}{r^2} + 3\frac{2Ml^2}{r^4} - 2\frac{l^2}{r^3} \overset{!}{=} 0$$
$$\Leftrightarrow \qquad\qquad (3M - r)l^2 = -Mr^2$$
$$\Leftrightarrow \qquad\qquad l^2 = \frac{Mr^2}{r - 3M} \tag{2.12}$$

As l^2 must be greater than 0, any circular timelike geodesic must fulfill $r > r_c = 3M$. In the limiting case $r = r_c$ the geodesics become lightlike; this marks the position of the unstable ($\partial_r^2 V_{\text{eff}}(r_c) < 0$) so-called *photon circle*.

2.3.2   q-metric

The most general axisymmetric, static and asymptotically flat solution of the vacuum field equations (see Eq. (2.5)) is represented by the Weyl class of solutions [11], the simplest of which is the Schwarzschild metric, which was described above.
For higher mass multipole moments, solutions from the Weyl class describing the exterior field are unhandy, making it difficult to solve analytically.

The so-called *q-metric* is an alternative, exact exterior solution of the field equations in vacuum. The metric can be written as

$$ds^2 = -\left(1 - \frac{2M}{r}\right)^{1+q} dt^2 + \left(1 - \frac{2M}{r}\right)^{-q} \cdot$$
$$\left[\left(1 + \frac{M^2 \sin^2 \vartheta}{r^2 - 2Mr}\right)^{-q(2+q)} \left(\frac{dr^2}{1 - \frac{2M}{r}} + r^2 d\vartheta^2\right) + r^2 \sin^2 \vartheta d\varphi^2\right] \tag{2.13}$$

where q is the dimensionless quadrupole parameter.

This axially symmetric and static solution reduces to the spherically symmetric Schwarzschild metric for $q = 0$. It is asymptotically flat for any fixed value of (q, M), and flat for $M \to 0$. It describes the exterior field of a spacetime with a naked singularity at $r = 2M$. [12]

Lightlike and timelike circular geodesics in the equatorial plane

In the following section, lightlike and timelike circular geodesics in the equatorial plane are subject to study. Similar to the Schwarzschild case, the effective potential can be obtained when solving the radial Euler-Lagrange equation. Circular motion with $\dot{r} \overset{!}{=} 0$ is equivalent to a test particle moving in the effective potential:

$$V_{\text{eff}} = \alpha^{q+1} \left[\frac{l^2}{r^2} \cdot \alpha^q + \varepsilon \right] \text{ with } \alpha := \left(1 - \frac{2M}{r} \right) \tag{2.14}$$

where $\varepsilon = 0$ for lightlike geodesics and $\varepsilon = 1$ for timelike geodesics and l is the specific angular momentum. [13]

The angular momentum of a test particle on a timelike circular orbit is obtained when looking at the extrema of the effective potential ($\partial_r V_{\text{eff}} = 0$):

$$\partial_r V_{\text{eff}} = \frac{2M(2q+1)l^2}{r^2} \alpha^{2q} - \frac{2l^2}{r^3} \alpha^{2q+1} + \frac{2(q+1)M}{r^2} \alpha^{q-1} \overset{!}{=} 0$$

$$\Leftrightarrow \quad 0 = \frac{rl^2 - 3Ml^2 - 2qMl^2}{M(q+1)\alpha^{-q}r^2}$$

$$\Leftrightarrow \quad l^2 = \frac{M(q+1)\alpha^{-q}r^2}{r - (3+2q)M} \tag{2.15}$$

As $l^2 > 0$ must be fulfilled, there is a critical circular orbit for which every lightlike circular orbit must be greater than

$$r > r_c = (3 + 2q)M \tag{2.16}$$

This reduces to $r = 3M$ for the Schwarzschild limit $q = 0$, as expected (see Eq. (2.12)). For positive values of q, it is strictly greater than the Schwarzschild radius, and decreases to $r \to 2M$ for decreasing values of q. In the limiting case $r = r_c$, the orbit becomes lightlike.

The marginally stable circular orbit can be obtained by either computing the extrema of the Keplerian specific angular momentum (see section 2.5.2, as well as section 4.3.2 and A.1), or by looking at the zeros of the second derivative of V_{eff}. Either way, the marginally stable circular orbit can be written as

$$r_{\text{MS}}^{\pm} = M \left(4 + 3q \pm \sqrt{5q^2 + 10q + 4} \right) \tag{2.17}$$

In contrast to the Schwarzschild case, there are two marginally stable circular orbits for a non-vanishing quadrupole moment.
This root in Eq. (2.17) has two zeros in $q = -1 \pm \sqrt{5}/5$; however, for $q > -0.5$, the marginally stable circular orbit is smaller than the critical orbit (Eq. (2.16)) and is thus discarded.
These limits split the spacetime into 3 regions:

   I $q > -0.5$

  II $-1 + \frac{\sqrt{5}}{5} \approx -0.553 < q < -0.5$

 III $q < -0.553$

Region I: $q > -0.5$

In this region, there is only one marginally stable orbit $r_{\mathrm{MS}}^+ > 2M$. All circular orbits in this region are stable. The lowest possible orbit reduces to $r_{\mathrm{MS}}^+(q = -0.5) = 3M$; however, in principal there is no upper limit.

Region II: $-0.553 \lesssim q < -0.5$

In this region, there are two marginally stable circular orbits $r_{\mathrm{MS}}^{\pm}$.
In the interval $r_{\mathrm{MS}}^- < r < r_{\mathrm{MS}}^+$, circular orbits are unstable. For radii $r > r_{\mathrm{MS}}^+$, circular orbits are stable.

Region III: $q \lesssim -0.553$

In this region, there are no marginally stable circular orbits. In principal, all circular orbits are allowed, starting at $r = 2M$. However, the angular momentum diminishes as the singularity is approached.

2.3.3 Erez-Rosen

The line element of a static mass with quadrupole moment can be described by the Erez-Rosen metric. [14, 15] This exact solution of the vacuum Einstein field equations (cf. Eq. (2.5)) belongs to the static Weyl class of solutions [11] and can be written in prolate spheroidal coordinates as

$$ds^2 = -f dt^2 + \frac{\sigma^2}{f} \left[e^{2\gamma}(x^2 - y^2) \left(\frac{dx^2}{x^2 - 1} + \frac{dy^2}{1 - y^2} \right) + (x^2 - 1)(1 - y^2)d\varphi^2 \right] \tag{2.18}$$

where σ is a constant and f and γ are functions of x and y, defined as

$$
\begin{aligned}
f =& \frac{x-1}{x+1} e^{-2qP_2Q_2} \\
\gamma =& \frac{1}{2}(1+q)^2 \ln \frac{x^2-1}{x^2-y^2} + 2q\,(1-P_2)\,Q_1 + q^2\,(1-P_2) \cdot \left[(1+P_2)\left(Q_1^2 - Q_2^2\right) \right. \\
& \left. + \frac{1}{2}\left(x^2-1\right)\left(2Q_2^2 - 3xQ_1Q_2 + 3Q_0Q_2 - Q_2'\right) \right]
\end{aligned}
$$

The functions $P_l(y)$ and $Q_k(x)$ are the Legendre functions of first and second kind respectively, and q is the dimensionless quadrupole parameter.
While x and y are very handy for computing the solution of the vacuum field equations, for the computation of the effective potential, the metric is transformed into Schwarzschild-like coordinates by

$$x = \frac{r}{M} - 1, \quad y = \cos \vartheta \tag{2.19}$$

and identifying σ as the mass of the central object M. For the calculations of the geometrically thick tori, the metric components g_{tt} and $g_{\varphi\varphi}$ are of importance. They transform like:

$$g_{tt} = -f = -\left(1 - \frac{2M}{r}\right)e^{-2qP_2Q_2} =: -\left(1 - \frac{2M}{r}\right)\beta \tag{2.20}$$

$$g_{\varphi\varphi} = \frac{M^2}{\left(1 - \frac{2M}{r}\right)\beta}\left(\frac{r^2}{M^2} - 2\frac{r}{M}\right)\sin^2\vartheta = \frac{r^2\sin^2\vartheta}{\beta} \tag{2.21}$$

with $P_2(\cos\vartheta) = \frac{1}{2}(3\cos^2\vartheta - 1)$ and $Q_2(r/M - 1) = \frac{1}{4}\left(\frac{3r^2}{M^2} - \frac{6r}{M} + 2\right)\ln\left[1 - \frac{2M}{r}\right] + \frac{3}{2}\left(\frac{r}{M} - 1\right)$ (2.22)

Lightlike and timelike circular geodesics in the equatorial plane

In the following section, lightlike and timelike circular geodesics are detailed. Motion fulfilling $\dot{r} \overset{!}{=} 0$ is equivalent to a test particle (or photon) moving in the effective potential

$$V_{\text{eff}} = f\left(\frac{f^2}{\sigma^2}\frac{l^2}{(x^2 - 1)} + \varepsilon\right) = \left(1 - \frac{2M}{r}\right)\beta_0\left[\beta_0\frac{l^2}{r^2} + \varepsilon\right] \tag{2.23}$$

where β_0 is given by

$$\beta_0 = \beta(\vartheta = \pi/2) = e^{qQ_2} \tag{2.24}$$

as $P_2(0) = -1/2$. The parameter ε determines the class of geodesics; for $\varepsilon = 0$, the geodesics are lightlike, for $\varepsilon = 1$, the geodesics are timelike. [16]
This reduces trivially to the effective potential in Schwarzschild spacetime (Eq. (2.11)) for $q = 0 \rightarrow \beta_0 = 1$.

The angular momentum of a test particle on a timelike circular orbit is obtained by calculating the extrema of the effective potential ($\partial_r V_{\text{eff}} = 0$).
After defining

$$\partial_r\beta_0 = q \cdot e^{qQ_2} \cdot \partial_r Q_2 =: q \cdot e^{qQ_2} \cdot u(r,q) \tag{2.25}$$

$$\text{with } u(r,q) = \frac{3}{2M}\left(\frac{r}{M} - 1\right)\ln\left[1 - \frac{2M}{r}\right] + \frac{3}{M} + \frac{M}{r(r - 2M)}, \tag{2.26}$$

the angular momentum can be expressed as (see section A.2.1 for the detailed calculation):

$$l^2 = \frac{\kappa(r,q)r^4}{2\beta_0}\frac{1}{r - M - \kappa(r,q)r^2} \quad \text{with } \kappa(r,q) = \left[\frac{2M}{r^2} + q\left(1 - \frac{2M}{r}\right)u(r,q)\right] \tag{2.27}$$

which reduces to the Schwarzschild limit in Eq. (2.12).
As β_0 is always greater than 0, the condition for the minimal radius of every timelike geodesics is given by the condition

$$r - M - \kappa(r,q)r^2 > 0 \tag{2.28}$$

In the limiting case $r - M - \kappa(r,q)r^2 = 0$, the geodesics become lightlike marking the position of the photon circle. Its behavior is depicted in figure 2.1.

As the quadrupole parameter increases, coming from $-\infty$, the minimal radius decreases. Until $q = 1$, there is only one photon circle. In the region $1 < q \lesssim 2.253$ there are two photon circles. The inner photon circle is stable, while the outer photon circle is unstable. Beyond $q > 2.253$, there is no photon circle covering the naked singularity anymore.
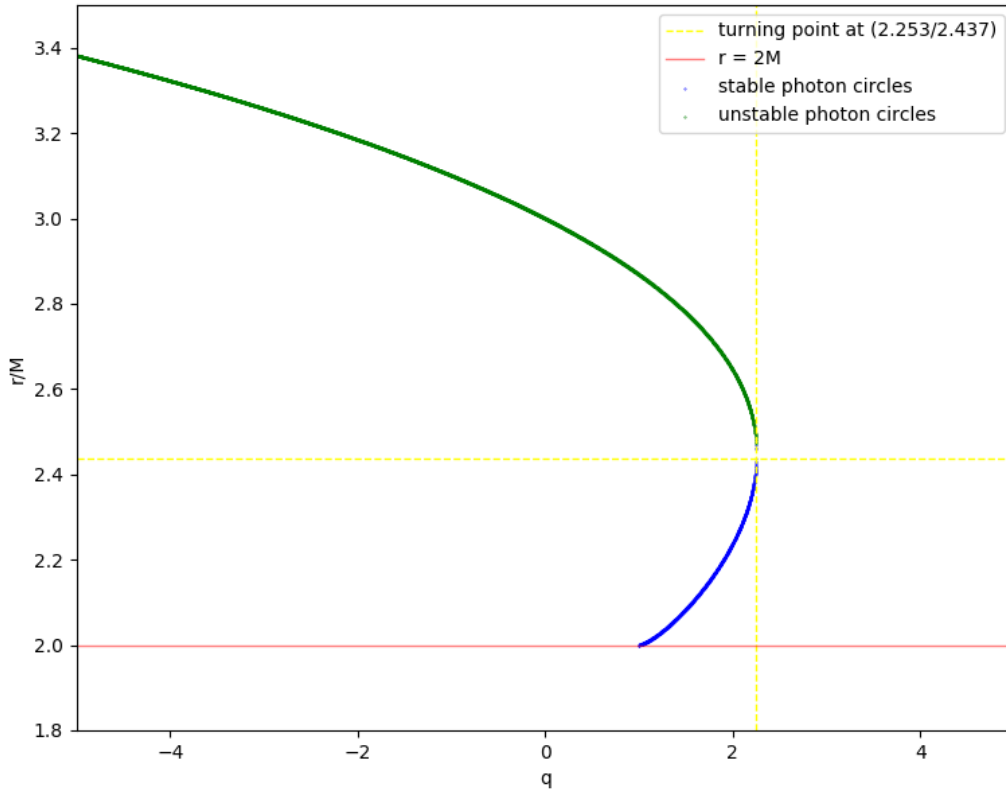
FIGURE 2.1: Limiting radius for lightlike geodesics, given by the condition in Eq. (2.28). The green graph indicates unstable orbits, while the blue graph indicates stable orbits.

2.4 Geometrically thick tori

In the following chapter, the theory of geometrically thick tori is discussed. In this context, the specific angular momentum is introduced, and the effective potential is established. [17, 18]

2.4.1 Von-Zeipel cylinders and specific angular momentum

The subject of study is the theoretical basis of perfect fluids around compact stellar objects. Therefore, an expression of a generic, stationary and axially symmetric metric is to be considered:

$$ds^2 = g_{tt}dt^2 + 2g_{t\phi}dtd\phi + g_{rr}dr^2 + g_{\vartheta\vartheta}d\vartheta^2 + g_{\varphi\varphi}d\varphi^2 \qquad (2.29)$$

This metric admits two Killing vectors. If the metric components are independent on the corresponding coordinate, the Killing vector can be expressed as a coordinate basis vector. This coordinate is called a *cyclic coordinate*. For this case, there are two Killing vectors for t and ϕ:

$$\eta^\mu = (1, 0, 0, 0), \qquad \xi^\mu = (0, 0, 0, 1) \qquad (2.30)$$

For circular motion ($u^r = u^\vartheta = 0$), the four-velocity can be written as

$$u^\mu = u^t(\eta^\mu + \Omega \xi^\mu),$$

where $\Omega = \frac{\mathrm{d}\varphi}{\mathrm{d}t}$ is the coordinate angular velocity.
From the normalising condition $g_{\mu\nu}u^\mu u^\nu = -1$, the four-velocity can be expressed in terms of the metric in (2.29):

$$(u^t)^{-2} = -g_{tt} - 2\Omega g_{t\varphi} - \Omega^2 g_{\varphi\varphi} \tag{2.31}$$

Following the definition of the *specific angular momentum* $l = -\frac{u_\varphi}{u_t}$, one can find an expression for the Euler equation:

$$\partial_\mu \ln |u_t| - \left(\frac{\Omega}{1 - \Omega l}\right) \partial_\mu l = -\frac{1}{\rho h}\partial_\mu p \tag{2.32}$$

where h is the relativistic specific enthalpy. [18]
Von-Zeipel cylinders are important for studying the effect of rotation on fluid constellations, as the centrifugal acceleration is perpendicular on the von-Zeipel surfaces. For a given constant angular momentum l_0, the determining equation for the von-Zeipel cylinders is given by:

$$l_0^2(g_{tt}\bar{g}_{t\varphi} - \bar{g}_{tt}g_{t\varphi}) + l_0(g_{tt}\bar{g}_{\varphi\varphi} - \bar{g}_{tt}g_{\varphi\varphi}) + g_{t\varphi}\bar{g}_{\varphi\varphi} - g_{\varphi\varphi}\bar{g}_{t\varphi} = 0, \tag{2.33}$$

$$\text{with } \bar{g} := g\left(r_0, \frac{\pi}{2}\right)$$

which reduces to $g_{tt}\bar{g}_{\varphi\varphi} - \bar{g}_{tt}g_{\varphi\varphi} = 0$ for any static spacetime. In this scenario, the von-Zeipel cylinders are independent on the specific angular momentum. [19]

2.4.2 Effective potential

If we assume barotropic fluids, the surfaces of constant l and Ω coincide and neither $\mathrm{d}\Omega$ nor $\mathrm{d}l$ possess a zero, the integration of the Euler equation (2.32) does not depend on the chosen path, thus

$$\mathcal{W} - \mathcal{W}_{in} := -\int_0^p \frac{\mathrm{d}p'}{\rho h} = \ln |u_t| - \ln |(u_t)_{in}| - \int_{l_{in}}^l \frac{\Omega}{1 - \Omega l'}\mathrm{d}l' , \tag{2.34}$$

where $\mathcal{W}$ is the *effective potential* and $\mathcal{W}_{in}$ the potential at the inner edge of the torus. [20, 21, 18]

The equation (2.34) simplifies if one chooses a fluid with constant specific angular momentum l. If one sets $\mathcal{W}_{in} = \ln |(u_t)_{in}|$, the equipotential surfaces are given by

$$\mathcal{W}(r, \vartheta) = \ln |u_t| \tag{2.35}$$
$$\text{with } (u_t)^{-2} = -\left(g^{tt} + 2lg^{t\varphi} + l^2 g^{\varphi\varphi}\right) \tag{2.36}$$

These two equations, (2.35) and (2.36), will be of most importance in the following computations. This will give insight in the dynamics and behavior of the fluid orbiting a compact stellar object.

2.5   Keplerian specific angular momentum and marginally stable/bound orbits

In this section, an analytical way of finding the limit values of the specific angular momentum is demonstrated. This procedure follows the approach depicted in Rezolla et.al, Relativistic Hydrodynamics. [18]

2.5.1   Keplerian specific angular momentum (KSAM)

For any stationary and axisymmetric object, the rotation law can be stated as

$$\Omega^2 \nabla_\mu g_{\varphi\varphi} + 2\Omega \nabla_\mu g_{t\varphi} + \nabla_\mu g_{tt} = 0 \tag{2.37}$$

This equation can be obtained by the condition that $u^\mu \nabla_\mu u^\nu = 0$ and considering circular motion with $u^\mu = u^t(\eta^\mu + \Omega \xi^\mu)$, where $\eta^\mu = \delta_t^\mu$, $\xi^\mu = \delta_\varphi^\mu$ are the Killing vectors associated with the spacetime.
Evaluating this equation in the equatorial plane, one receives the Keplerian angular velocity (*also*: Keplerian frequency) Ω_K.

For any *static* spacetime ($g_{t\varphi} = 0$) and considering $\Omega = \frac{u^\varphi}{u^t}$ and $l = -\frac{u_\varphi}{u_t}$, the relation between the Keplerian angular velocity and the Keplerian specific angular momentum l_K can be written as

$$\Omega_K^2 = \left(\frac{u^\varphi}{u^t}\right)^2 = \left(\frac{g^{\varphi\varphi}u_\varphi + g^{\varphi t}u_t}{g^{tt}u_t + g^{t\varphi}u_\varphi}\right)^2 \tag{2.38}$$

$$= \left(\frac{g^{\varphi\varphi}u_\varphi}{g^{tt}u_t}\right)^2 = \left(\frac{g^{\varphi\varphi}}{g^{tt}}\right)^2 l_k^2 \tag{2.39}$$

With Eq. (2.37) and (2.39), the Keplerian specific angular momentum (KSAM) can be computed, given the co- and contravariant time- and angular components of the metric. [18, 22]

2.5.2   Marginally stable orbit and specific angular momentum

The marginally stable circular orbit r_{MS} is defined as the radius where the KSAM becomes minimal:

$$r_{\text{MS}} = r\big|_{\partial_r l_K = 0} \tag{2.40}$$

Accordingly, the marginally stable specific angular momentum l_{MS} is defined as

$$l_{\text{MS}} = l_K(r = r_{\text{MS}}) \tag{2.41}$$

2.5.3   Marginally bound orbit and specific angular momentum

The marginally bound circular orbit r_{MB} can be found when looking at the extrema of the effective potential approach when considering geodesics. This effective potential V_{eff} is found by computing the differential equation in time for r in the equatorial plane.

The condition for finding an extremum $\partial_r V_{\text{eff}} = 0$ leads to a relation for the angular momentum l_{extr}. When inserting this back into the effective potential, $V_{\text{eff}}(l_{\text{extr}}) =: V_{\text{extr}} \stackrel{!}{=} 1$ marks the position of the marginally bound orbit:

$$r_{\text{MB}} = r\big|_{V_{\text{extr}}=1} \tag{2.42}$$

Accordingly, the marginally bound specific angular momentum l_{MB} is given as the KSAM, evaluated at the marginally bound orbit:

$$l_{\text{MB}} = l_K(r = r_{\text{MB}}) \tag{2.43}$$

Chapter 3

Tori in Schwarzschild spacetime

In the following chapter, the properties and behavior of perfect fluids, in particular geometrically thick tori, are studied.

As most of the calculations involve metric components, the explicit form of the metric is recalled as (cf.(2.9)):

$$ds^2 = -\left(1 - \frac{2M}{r}\right)dt^2 + \left(1 - \frac{2M}{r}\right)^{-1}dr^2 + r^2(d\vartheta^2 + \sin^2\vartheta d\varphi^2) \tag{3.1}$$

This chapter follows the approach of computing geometrically thick tori given in *Relativistic Hydrodynamics*, Rezolla et.al. [18], as tori in Schwarzschild spacetime are extensively studied.

3.1 Von-Zeipel cylinders in Schwarzschild spacetime

In this section, the von-Zeipel cylinders are calculated for a central object that can be described by the Schwarzschild metric. They give an insight on the behavior of fluids in circular motion around a massive object.

The condition for the equipotential surfaces is given in Eq. (2.33), and can be expressed as

$$g_{tt}\bar{g}_{\varphi\varphi} - \bar{g}_{tt}g_{\varphi\varphi} \overset{!}{=} 0 \quad \text{with} \quad \bar{g} = g(r = r_0, \vartheta = \pi/2) \tag{3.2}$$

$$\Leftrightarrow \quad \frac{r_0 - 2M}{r_0}r^2\sin^2\vartheta = \frac{r - 2M}{r}r_0^2 \tag{3.3}$$

$$\Rightarrow \quad \sin^2\vartheta = \frac{r_0^3}{r^3}\cdot\frac{r - 2M}{r_0 - 2M} \tag{3.4}$$

The plot of von-Zeipel cylinders for different constant values of r_0 is depicted in figure 3.1. Each blue line represents the solution of Eq. (3.4) for different constant r_0. For $r_0 > 3M$, there are two distinct surfaces, one in the vicinity of $r = 2M$, one outside of $r = 3M$. The outer surfaces bend towards $r = 3M$; the curvature is largest in the equatorial plane. For increasing distance to the central object, the equipotential lines become increasingly less curved.

In the limiting case $r = 3M$, there is a equipotential surfaces that crosses $r = 3M$ and connects the inner and outer surfaces.
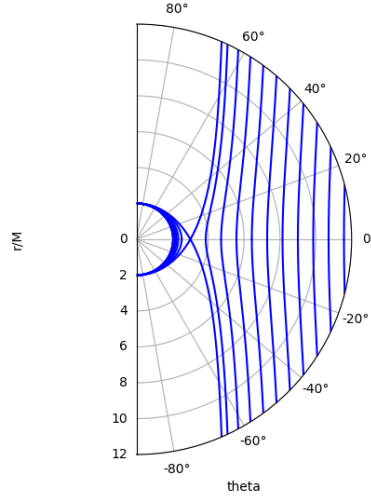
FIGURE 3.1: Depiction of von-Zeipel cylinders in Schwarzschild spacetime. The different blue lines indicate equipotential surfaces for different values of r_0.

3.2   Effective potential

In this section, geometrically thick tori are computed in Schwarzschild spacetime. For computation purposes, the contravariant metric elements are needed:

$$g^{tt} = -\left(1 - \frac{2M}{r}\right)^{-1}, \; g^{t\varphi} = 0, \; g^{\varphi\varphi} = \frac{1}{r^2 \sin^2 \vartheta} \tag{3.5}$$

The $g^{t\varphi}$-term vanishes, as the Schwarzschild spacetime is static.
With this, computing the four-velocity in (2.36) gives:

$$u_t = \sqrt{\frac{(r-2)r^2 \sin^2 \vartheta}{r^3 \sin^2 \vartheta - l^2(r-2)}}, \tag{3.6}$$

and so the equipotential surfaces (*cf.*, Eq. (2.35)) follow accordingly (see also *Relativistic Hydrodynamics*, Rezolla et. al. [18]):

$$\mathcal{W}(r,\vartheta) = \frac{1}{2} \ln \left[\frac{(r-2)r^2 \sin^2 \vartheta}{r^3 \sin^2 \vartheta - l^2(r-2)} \right] \tag{3.7}$$

To analyze the stability and behavior, the dependence of the effective potential on the radius is investigated. In figure 3.2, the effective potential in the equatorial plane ($\vartheta = \pi/2$) and for constant l is shown.
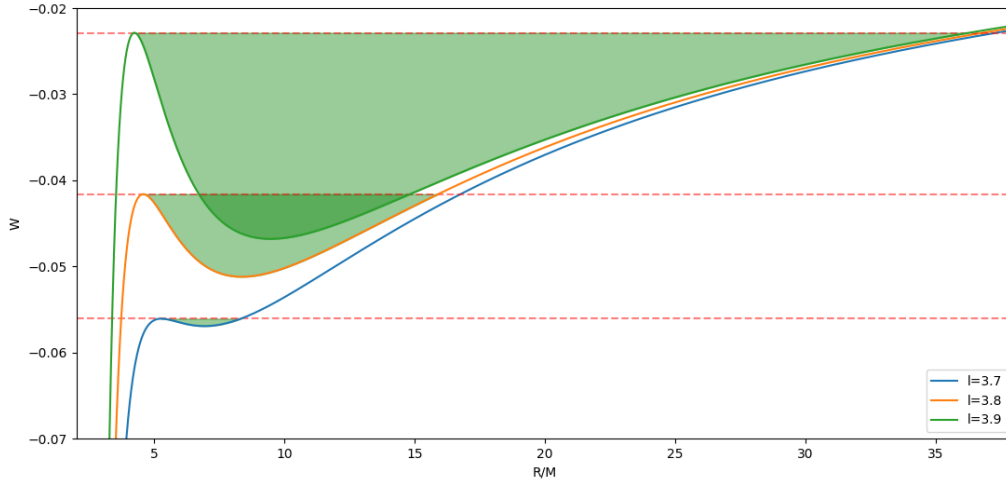
FIGURE 3.2: Representative behavior of the effective potential, in dependence of
r/M, in the equatorial plane and fixed $l = 3.8$. The green filled area indicates the
maximum region that can be filled by the fluid.

The figure illustrates the outermost closed equipotential surface of the torus; the fluid can
occupy the region that is shaded in green. The intersections of the red dotted line and the po-
tential mark the location of the minimal inner edge and the maximal outer edge of the torus.
The area indicated by these two points is called its *Roche lobe*.
For increasing values of l, the height of the cusp, and consequently the extension of the torus
into space, increases. While the position of the cusp remains the same, the position of the local
minimum moves to higher values of r/M. Furthermore, the ratio of the effective potential at
the maximum, compared to the minimum, increases with higher values of l.
These impacts on the effective potential can be explained by the increased centrifugal effects,
associated with higher specific angular momentum.

The geometry of these tori can be seen more clearly in figure 3.3. Solving equation (3.7) for
ϑ yields:

$$\vartheta = \arcsin\left(\pm\sqrt{\frac{(2-r)\omega l^2}{(1-\omega)r^3 - 2r^2}}\right), \quad \omega = e^{2\cdot\mathcal{W}} \tag{3.8}$$

The different colored lines correspond to different values of $\mathcal{W}$, representing tori that are not
filled all the way to their *Roche lobe*. As none of these potential surfaces cross the event horizon
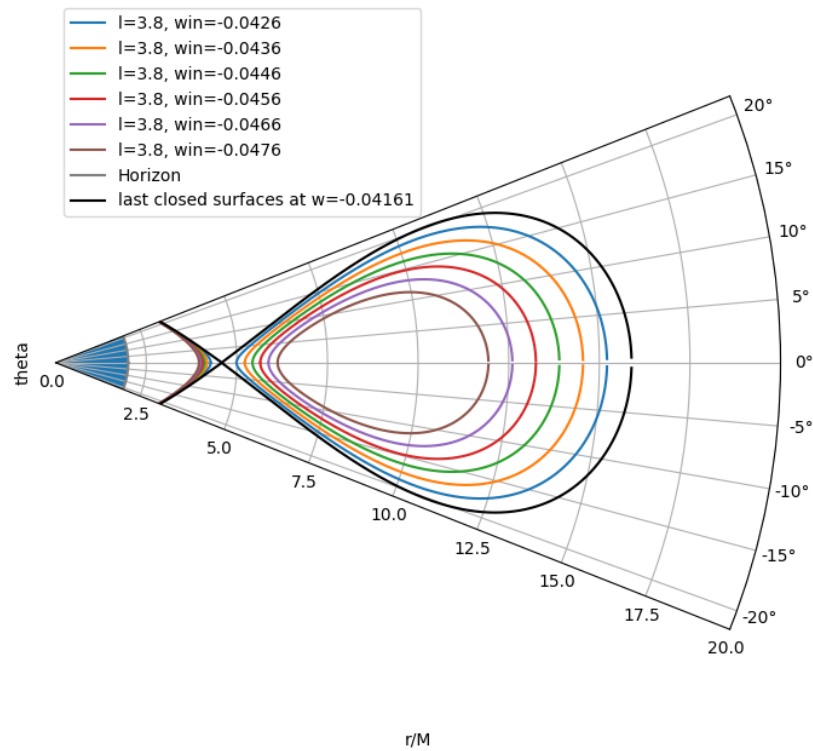at $r/M = 2$, they are considered closed.

FIGURE 3.3: Equipotential surfaces of geometrically thick tori with constant $l = 3.8$, depending on the angle ϑ. Each line represents a torus for different values of $\mathcal{W}$; the horizon of the Schwarzschild-black hole extends to $r/M = 2$.

Runaway instability [18]

If mass is added to the fluid, exceeding the Roche limit, it flows through the cusp and is forced on unstable orbits. The fluid is thus forced to accrete onto the black hole, increasing the mass of the black hole. This process moves the position of the cusp; two possible scenarios are conceivable.

If the position of the cusp would move to a smaller value of r, the accretion would stop, granting stability. If the position of the cusp would move to increasing values of r, the accretion process would accelerate, triggering what is usually called the *runaway instability*.

This is still a topic of current studies, but current simulations suggest that the tori are stable under astrophysically realistic conditions.

3.3 Limits to the specific angular momentum

In this section, the limits of the specific angular momentum for a torus in Schwarzschild space-time is discussed, based on the theory in section 2.5.

3.3.1 Keplerian specific angular momentum

First, the Keplerian angular velocity is computed, following Eq. (2.37). The covariant metric components are taken from Eq. (2.9), and evaluated in the equatorial plane:

$$\Omega^2 \nabla_\mu g_{\varphi\varphi} + \nabla_\mu g_{tt} = 0$$

$$\Leftrightarrow \qquad \Omega_K^2 \cdot \partial_r r^2 = \partial_r \left(1 - \frac{2M}{r} \right)$$

$$\Leftrightarrow \qquad \Omega_K^2 = \frac{M}{r^3} \tag{3.9}$$

The contravariant metric components in the equatorial plane are given as $g^{tt} = r^{-2}$ and $g^{\varphi\varphi} = \left(1 - \frac{2M}{r} \right)^{-1}$. Thus, following Eq. (2.39):

$$\Omega_K^2 = \left(\frac{g^{\varphi\varphi}}{g^{tt}} \right)^2 \cdot l_K^2$$

$$\Leftrightarrow \frac{M}{r^3} = \frac{(1 - \frac{2M}{r})^2}{r^4} \cdot l_K^2$$

$$\Leftrightarrow Mr^3 = (r - 2M)^2 \cdot l_K^2$$

$$\Leftrightarrow \quad l_K^2 = \frac{Mr^3}{(r - 2M)^2} \tag{3.10}$$

This expression is necessary for the computation of the marginally stable- and marginally bound specific angular momentum.

3.3.2 Marginally stable specific angular momentum

Next, the marginally stable orbit r_{MS} is computed. For this, we need the position of the minimum of l_K (cf. Eq. (2.40)):

$$\partial_r l_K = \partial_r \sqrt{\frac{Mr^3}{(r - 2M)^2}} = 0$$

$$\Leftrightarrow \quad \frac{3\sqrt{Mr}}{2(r - 2M)} - \frac{\sqrt{Mr^3}}{(r - 2M)^2} = 0$$

$$\Leftrightarrow \frac{3}{2}\sqrt{Mr}(r - 2M) - \sqrt{Mr} \cdot r = 0 \ \Big| \ r \neq 0$$

$$\Leftrightarrow \qquad \frac{3}{2}(r - 2M) - r = 0$$

$$\Leftrightarrow \qquad r_{ms} = 6M \tag{3.11}$$

Given this, the marginally stable specific angular momentum l_{MS} can be expressed as (see Eq. (2.41)):

$$l_{MS} = l_K(r = r_{MS}) = \frac{3}{2}\sqrt{6}M \approx 3.674M \tag{3.12}$$

This marks the lower limit of the specific angular momentum for the geometrically thick tori. For $l < l_{MS}$, there are no closed surfaces, as there is no local maximum in the effective potential anymore. A fluid with $l < l_{MS}$ would accrete onto the black hole.

3.3.3 Marginally bound specific angular momentum

To find the marginally bound orbit, the minimum of the effective potential (see Eq. (2.11)) needs to be observed; this results in a condition for the angular momentum for a test particle (see section 2.3.1 and Eqs. (2.11) and in particular (2.12)):

$$V_{eff} = \left(1 - \frac{2M}{r}\right)\left(1 + \frac{l^2}{r^2}\right)$$
$$l^2 = \frac{Mr^2}{r - 3M} \tag{3.13}$$

Following the condition that l^2 cannot be smaller than 0, every bound orbit has to be greater than 3M, with the critical orbit $r = 3M$ marking the position of the photon sphere.
Inserting this back into the effective potential shows the values at the local extrema; setting $V_{eff} \overset{!}{=} 1$ marks the position of the marginally bound orbit r_{MB}:

$$V_{extr} = \left(1 - \frac{2M}{r}\right)\left(\frac{M}{r - 3M} + 1\right) \overset{!}{=} 1$$
$$\Leftrightarrow \quad 1 - \frac{2M^2}{r(r - 3M)} + \frac{M}{r - 3M} - \frac{2M}{r} = 1$$
$$\Leftrightarrow \quad \frac{-2M^2 + Mr - 2M(r - 3M)}{r(r - 3M)} = 0$$
$$\Leftrightarrow \quad -2M^2 + Mr - 2Mr + 6M^2 = 0$$
$$\Leftrightarrow \quad r_{MB} = 4M \tag{3.14}$$

With this, the marginally bound specific angular momentum l_{MB} can be found as the value of l_K at the marginally bound radius:

$$l_{MB} = l_K(r = r_{MB}) = 4M \tag{3.15}$$

This marks the upper limit for the specific angular momentum for geometrically thick tori. For $l > l_{MB}$, there are no closed surfaces, as the value of the effective potential at the cusp is not the local-, but the global maximum. There is no local minimum anymore; any fluid with $r < r_{cusp}$ must accrete onto the black hole, and any fluid with $r > r_{cusp}$ will escape into infinity.

Summary

In this section, the upper and lower limit of the specific angular momentum were computed. For geometrically thick tori in Schwarzschild spacetime, there exist closed tori for $l_{MS} = 3.67M < l < 4M = l_{MB}$.

Chapter 4

Tori in q-metric

In this chapter, the properties and behavior of perfect fluids,in particular geometrically thick tori, are studied.

As most of the calculations involve metric components, the explicit form of the metric is recalled as (cf.(2.13)):

$$ds^2 = -\left(1 - \frac{2M}{r}\right)^{1+q} dt^2 + \left(1 - \frac{2M}{r}\right)^{-q} \cdot$$
$$\left[\left(1 + \frac{M^2 \sin^2 \vartheta}{r^2 - 2Mr}\right)^{-q(2+q)} \left(\frac{dr^2}{1 - \frac{2M}{r}} + r^2 d\vartheta^2\right) + r^2 \sin^2 \vartheta d\varphi^2\right] \tag{4.1}$$

4.1   Von-Zeipel cylinders in q-metric

In this section, the von-Zeipel cylinders are calculated in the q-metric. They give an insight on the behavior of fluids in circular motion around a massive object.

As for any static spacetime, the cylinders are independent on the specific angular momentum. The determining equation is given by Eq. (2.33):

$$g_{tt}\bar{g}_{\varphi\varphi} - \bar{g}_{tt}g_{\varphi\varphi} = 0, \; g_{tt} = -\alpha^{1+q}, \; g_{\varphi\varphi} = \alpha^{-q}r^2 \sin^2 \vartheta \tag{4.2}$$

$$\text{with } \alpha := \left(1 - \frac{2M}{r}\right) \text{ and } \bar{g}_{\mu\nu} := \bar{g}_{\mu\nu}(r = r_0, \vartheta = \pi/2)$$

$$\Rightarrow \sin^2 \vartheta = \frac{r_0^2}{r^2} \cdot \frac{\alpha^{1+2q}}{\alpha_0^{1+2q}} \text{ with } \alpha_0 := \alpha(r_0, \pi/2) \tag{4.3}$$

The cylinders for varying r_0 and quadrupole parameter q can be seen in figure 4.1.

Every line represents the solution of Eq. (4.3) for a different r_0. In the Schwarzschild limit $q = 0$, there is a crossing surface for $r_{cr} = 3M$. This radius increases for $q > 0$ and decreases for $q < 0$. For $q < -0.5$, there is no crossing surface, and for $q < -1$, there are closed surfaces for $r < 2M$.

The equipotential lines become increasingly curved for positive values of q, while the curvature for negative values of the quadrupole parameter is only relevant in the vicinity of $r = 2M$.
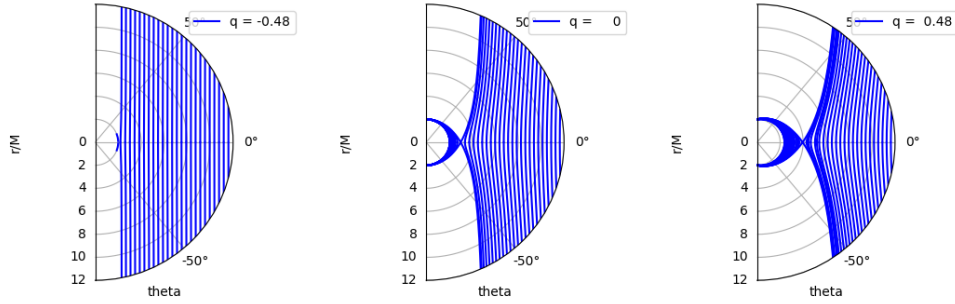
FIGURE 4.1: Von-Zeipel cylinders for different values of the quadrupole param-
eter q. Each line indicates a potential surface at a constant r_0. Left: $q = -0.48$;
mid: $q = 0$, Schwarzschild limit; right: $q = 0.48$

4.2 Effective potential

In this section, geometrically thick tori are computed in q-metric. For the computation of the effective potential, the contravariant metric elements are needed:

$$g^{tt} = -\alpha^{-(1+q)}, \ g^{t\varphi} = 0, \ g^{\varphi\varphi} = \frac{\alpha^q}{r^2 \sin^2 \vartheta} \ \text{ with } \alpha := \left(1 - \frac{2M}{r}\right) \tag{4.4}$$

Again, the $g^{t\varphi}$ vanishes as the spacetime is static.
The four-velocity (cf. Eq. (2.36)) can thus be expressed as

$$
\begin{aligned}
u_t^{-2} &= -\left(-\alpha^{-(1+q)} + l^2 \frac{\alpha^q}{r^2 \sin^2 \vartheta}\right) \\
&= \frac{\alpha^{-(1+q)} r^2 \sin^2 \vartheta - l^2 \alpha^q}{r^2 \sin^2 \vartheta}
\end{aligned}
$$

With this, the effective potential (cf. (2.35)) is given by

$$\mathcal{W}(r, \vartheta) = \frac{1}{2} \ln \left[\frac{r^2 \sin^2 \vartheta}{\alpha^{-(1+q)} r^2 \sin^2 \vartheta - l^2 \alpha^q} \right] \tag{4.5}$$

To analyze the extension and behavior, the dependence of the effective potential on the radius for different values of q is investigated. In figure (4.2), the effective potential in the equatorial plane ($\vartheta = \pi/2$) for 3 different values of q and constant l are shown.

Similar to the Schwarzschild case, the outermost closed equipotential surface of the torus is indicated by the blue dashed line. The intersection of this line and the effective potential marks the location of the cusp and the outer edge of the torus, the green shaded area indicates the Roche limit of the respective effective potential.
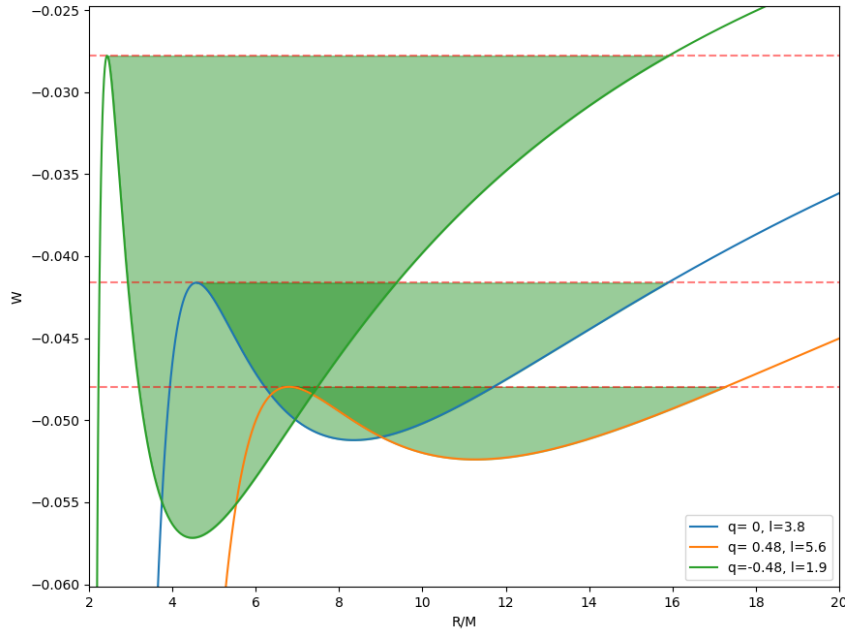The geometry of these tori can be seen more clearly in figure 4.3.

FIGURE 4.2: Representative behavior of the effective potential in the equatorial plane for 3 different values of q. Left: effective potential with $q = -0.48$, $l = 1.9$; mid: effective potential with $q = 0$, $l = 3.8$ (Schwarzschild limit); right: effective potential with $q = 0.48$, $l = 5.6$. The green shaded area represents the Roche limit of the respective effective potential.

Solving Eq. (4.5) for constant $\mathcal{W}$ and defining $\omega := e^{2\mathcal{W}}$:

$$e^{2 \cdot \mathcal{W}} = \frac{r^2 \sin^2 \vartheta}{\alpha^{-(1+q)} r^2 \sin^2 \vartheta - l^2 \alpha^q}$$

$$\Leftrightarrow r^2 \sin^2 \vartheta = \omega \alpha^{-(1+q)} r^2 \sin^2 \vartheta - \omega \alpha^q l^2$$

$$\Leftrightarrow \quad \sin^2 \vartheta = \frac{\omega \alpha^q l^2}{\omega \alpha^{-(1+q)} r^2 - r^2}$$

$$\Rightarrow \qquad \vartheta = \arcsin\left(\pm \sqrt{\frac{\omega \alpha^q l^2}{\omega \alpha^{-(1+q)} r^2 - r^2}} \right) \qquad (4.6)$$

This polar dependency can be seen in figure (4.3). The different colors represent the polar dependency of the effective potential for three different values of the quadrupole parameter. The influence of the quadrupole parameter on the effective potential is be discussed in detail in section 4.4.
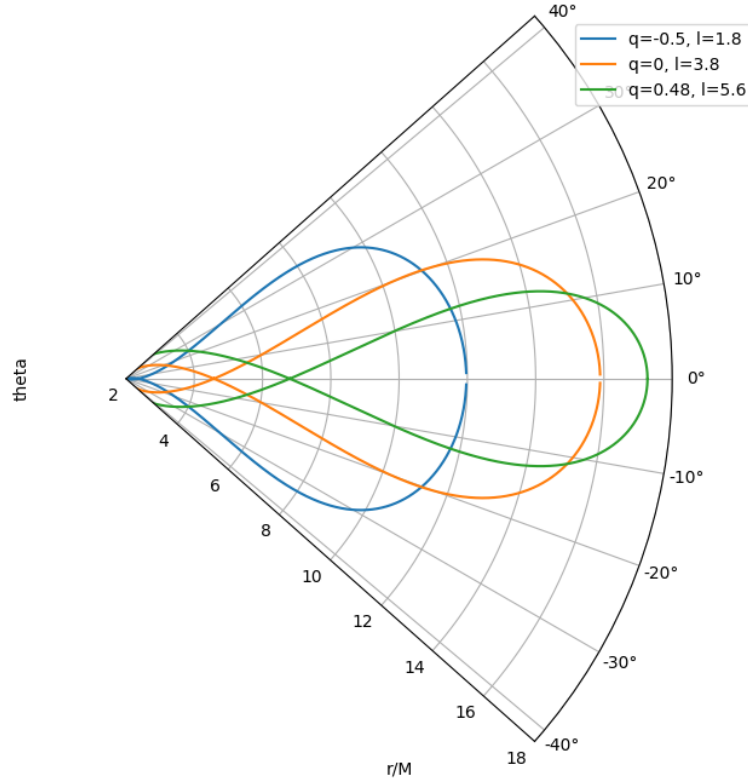
FIGURE 4.3: Polar dependency of the effective potential on the radius, depicted
for three different values of q. Depicted is the Roche limit for a given q and l.

4.3 Limits to the specific angular momentum

In this section, the upper and lower limits of the specific angular momentum are computed.
Thus first, an expression for the Keplerian specific angular momentum is needed. For any
major quantity, there will be a short substantiation on the Schwarzschild limit $q = 0$.

4.3.1 Keplerian specific angular momentum

Here, the Keplerian specific angular momentum (KSAM) is computed (see section 2.5).
First, the Keplerian angular frequency is computed following Eq. 2.37:

$$\Omega_K^2 \nabla_\mu g_{\varphi\varphi} + \nabla_\mu g_{tt} = 0$$

$$\Leftrightarrow \quad \Omega_K^2 \partial_r(\alpha^{-q} r^2) + \partial_r(-\alpha^{q+1}) = 0$$

$$\Leftrightarrow \Omega_K^2 \left[-\frac{2M}{r^2} q \alpha^{-q-1} r^2 + 2r\alpha^{-q} \right] = \frac{2M}{r^2}(1+q)\alpha^q$$

$$\Leftrightarrow \quad \Omega_K^2 \left[-Mq\alpha^{-1} + r \right] = \frac{M(q+1)}{r^2}\alpha^{2q}$$

$$\Leftrightarrow \qquad \Omega_K^2 = \frac{M(q+1)\alpha^{2q}}{r^2(r - Mq\alpha^{-1})} \qquad (4.7)$$

For $q = 0$, this expression reduces trivially to the Schwarzschild Keplerian angular momentum $\Omega_K^2 = \frac{M}{r^3}$.

Having obtained the Keplerian angular frequency, the KSAM can be computed, taking into account the contravariant metric components in Eq. (4.4):

$$\frac{g^{\varphi\varphi}}{g^{tt}} = \frac{\alpha^{1+2q}}{r^2} \tag{4.8}$$

$$\Rightarrow \Omega_K^2 = \left(\frac{g^{\varphi\varphi}}{g^{tt}}\right)^2 \cdot l_K^2 = \frac{\alpha^{2(1+2q)}}{r^4} l_K^2 \tag{4.9}$$

$$\Leftrightarrow l_K^2 = \frac{r^4}{\alpha^{2(1+2q)}} \frac{M(q+1)\alpha^{2q}}{r^2(r - Mq\alpha^{-1})} \tag{4.10}$$

$$\Leftrightarrow l_K^2 = \frac{r^2(q+1)M}{\alpha^{2(q+1)}(r - Mq\alpha^{-1})} \tag{4.11}$$

Schwarzschild limit $q = 0$

Considering the Schwarzschild limit $q = 0$ and $(1 - 2M/r)^{-1} = r/(r - 2M)$, Eq. (4.11) reduces to the Schwarzschild KSAM (cf. Eq. (3.10)):

$$l_K^2(q = 0) = \frac{r^2 M}{\alpha^2 r} = rM \frac{r^2}{(r - 2M)^2} = \frac{Mr^3}{(r - 2M)^2}$$

4.3.2 Marginally stable specific angular momentum

To compute the marginally stable circular orbit, the position of the minimum of l_K is to be calculated. For the exact computation, see Appendix A.1. The marginally stable circular orbit is then given by:

$$r_{MS}^{\pm} = M\left(4 + 3q \pm \sqrt{5q^2 + 10q + 4}\right) \tag{4.12}$$

There are two marginally stable orbits (see section 2.3.2 for more detail).
Having a look at the root, one can see that there are 2 zeros at $q = -1 \pm \sqrt{5}/5$. The solution with the minus sign is smaller than $q = -1$ and thus discarded as a consequence of the condition that r_{MS} must be real (see appendix section A.1.1 for details).
The remaining critical value is thus $q \approx -0.553$.
For the region $q > -0.5$, the r_{ms}^- solution is discarded, as the radius becomes smaller than the critical circular orbit (see Eq. (2.16)). However, in the region $-0.553 \lesssim q < -0.5$, both r_{MS}^+ and r_{MS}^- are permitted.

The dependence of the marginally stable circular orbit r_{MS} and marginally stable specific angular momentum l_{MS} on q can be seen in figure (4.4).
In the region $-0.553 \lesssim q < -0.5$, there are two values allowed for l_K. The two $l_K(r = r_{MS}^-)$ and $l_K(r = r_{MS}^+)$ merge at $(q, l) = (-0.553, 1.495)$. The maximum of angular momentum $l_{MS}(r = r_{MS}^-)$ cuts off at $(q, l) = (-0.5, 2)$.
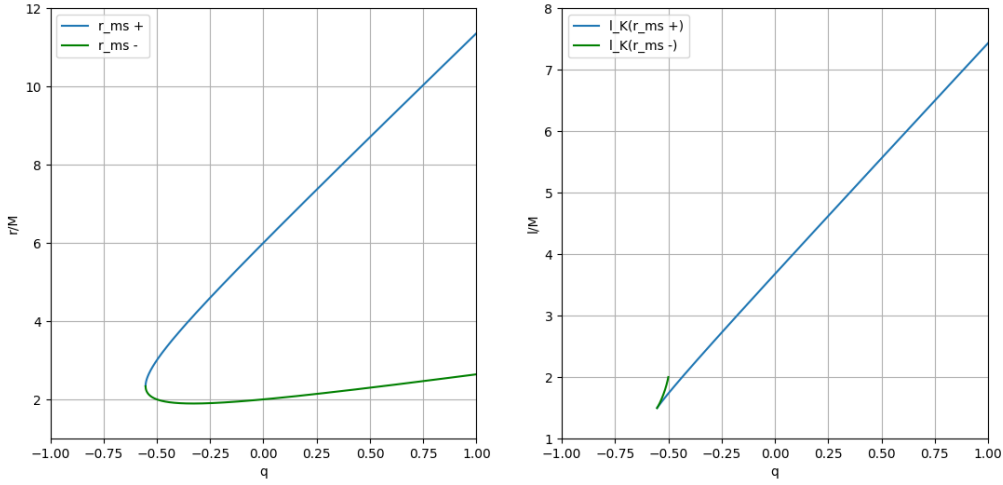
FIGURE 4.4: Plot of the marginally stable circular orbit and marginally stable specific angular momentum, depending on the quadrupole parameter q. Left: $r_{\mathrm{MS}}^{\pm}$ depending on q; right: l_{MS} depending on q. The reason of the cut-off is that l_K^2 becomes negative for r_{MS}^- and $q > -0.5$.

4.3.3 Marginally bound specific angular momentum

Next, the marginally bound circular orbit is calculated, following the approach detailed in section (2.5). For this, one needs to compute the extrema of the effective potential (see Eq. (2.42)). Recalling both from chapter 1, Eqs. (2.14) and (2.15):

$$V_{\mathrm{eff}} = \alpha^{q+1}\left(\frac{l^2}{r^2}\alpha^q + 1\right)$$

$$\Rightarrow \quad l^2 = \frac{M(q+1)\alpha^{-q}r^2}{r - (3+2q)M} \tag{4.13}$$

Again, for $q = 0$, this reduces trivially to the Schwarzschild limit of Eq. (3.13).
This equation sets the condition that every circular orbit must be greater than $r_{\mathrm{crit}} = (3+2q)M$ so that l^2 is greater than 0.
For computing the marginally bound circular orbit, l^2 from Eq. (4.13) is reinserted into V_{eff} to calculate V_{extr}; setting $V_{\mathrm{extr}} \overset{!}{=} 1$ marks the position of the marginally bound orbit r_{MB}:

$$\frac{\alpha^{q+1}M(q+1)}{r - (3+2q)M} + \alpha^{q+1} - 1 = 0$$

There is no analytical solution for this equation, thus r_{MB} (and, thus subsequently, l_{MB}) is numerically calculated and is displayed in figure (4.5).

Summary

In this section, the upper and lower limit of the specific angular momentum were calculated. There are two marginally stable specific angular momenta $l_{\mathrm{MS}}^{\pm}$ for $-0.553 \lesssim q < -0.5$, serving as the upper and lower limit for the specific angular momentum respectively. For $q > -0.5$, there is one l_{MS} and l_{MB}. There are closed equipotential surfaces only for pairs of values (q, l), enclosed by the curves seen in figure (4.6).
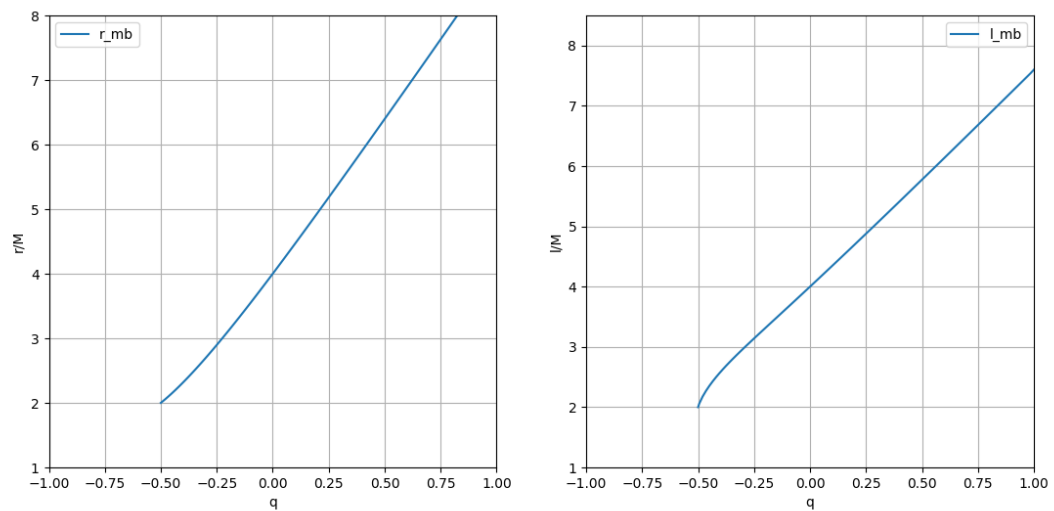
FIGURE 4.5: Numerical depiction of the marginally bound circular orbit (left) and marginally bound specific angular momentum (right) depending on the quadrupole parameter q.

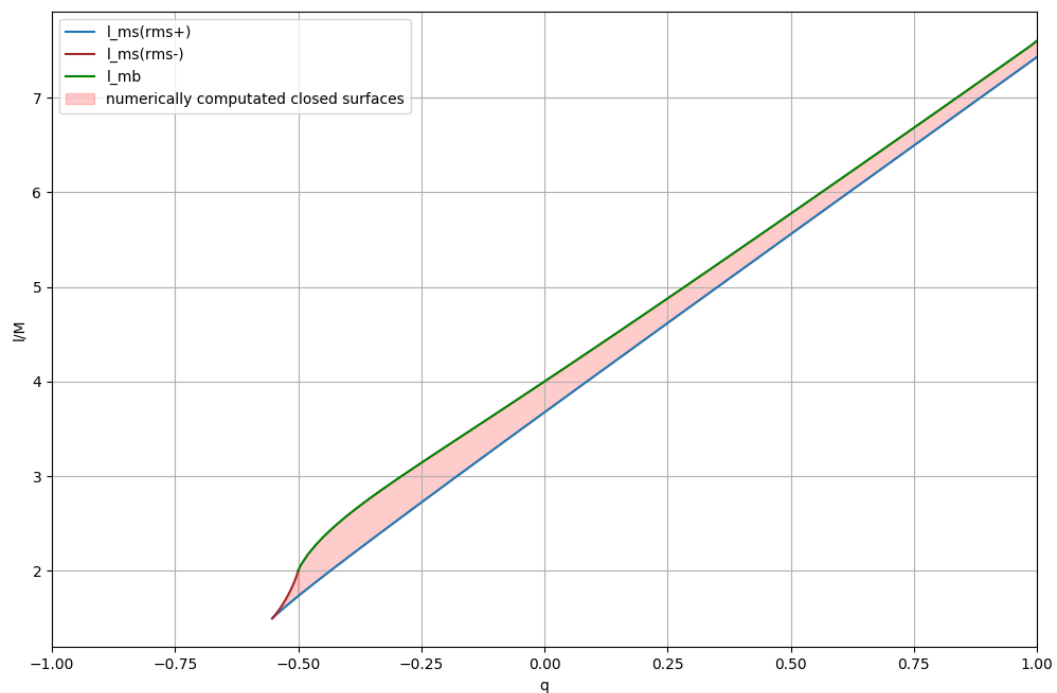

FIGURE 4.6: Course of both marginally stable specific angular momenta and the marginally bound angular momentum. Only values (q, l), enclosed by these curves (red shaded) are closed result in closed equipotential surfaces.

4.4 Influence of the quadrupole parameter on the behavior of the tori

In this section, the influence of the quadrupole parameter on the behavior of the tori is discussed in detail. The general geometrical properties can be seen in figure 4.2 and 4.3.
Compared to the Schwarzschild limit ($q = 0$, blue graph in figure 4.2) , the course of the effective potential for geometrically thick tori with non-vanishing quadrupole moment does not change significantly, possessing a local minimum and maximum.
However, the influence of the quadrupole parameter on the effective potential can be seen when observing the position of the cusp.
For increasing values of q, the cusp moves to increasing values of r, approaching $r = 2M$ for decreasing values of q. Additionally, the relative difference between the effective potential of the cusp and local minimum decreases for increasing values of q.
When looking at figure 4.3 in particular, one can see that the tori extend to greater values of r for increasing values of q. In addition to that, the equipotential surfaces extend to higher values of ϑ in the presence of an object with negative quadrupole moment.
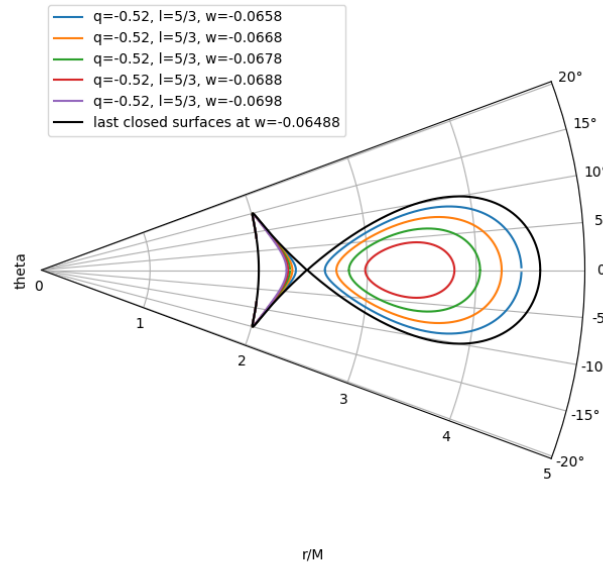

FIGURE 4.7: Polar dependency of the effective potential on the radius for the quadrupole parameter q in the region $-0.553 \lesssim q < -0.5$. Shown is the behavior of the geometrically thick torus for $q = -0.52$ and specific angular momentum $l = 5/3$. The different colored lines represent tori not filling their Roche limit.

Geometrically thick tori in the region $-0.553 \lesssim q < -0.5$

Contrary to the Schwarzschild case, for values of the quadrupole parameter $-0.553 \lesssim q < -0.5$ there is no marginally bound, but two marginally stable specific angular momenta. Tori with a quadrupole parameter within this range differ geometrically; see figure 4.7 for a graphic representation.
In this region, there are two closed surfaces, as $\mathcal{W} \to \infty$ for $r \to 2M$. The cusp acts as the dividing line, splitting the torus into an inner and an outer torus. The inner edge of the inner torus is greater than $r = 2M$. For a torus filling its Roche lobe, the distance between the two tori is infinitesimally small; otherwise, the two tori are physically separated.

Chapter 5

Tori in Erez-Rosen spacetime

5.1 Von-Zeipel cylinders in Erez-Rosen spacetime

In this section, the von-Zeipel cylinders are calculated for a central object that can be described by the Erez-Rosen metric. They give an insight on the behavior of fluids in circular motion around a massive object.

As for any static and axisymmetric spacetime, the cylinders are independent on the specific angular momentum. The determining equation for the equipotential surfaces is given by Eq. (2.33); the covariant metric components are taken from Eq. (2.20) and (2.21):

$$g_{tt}\bar{g}_{\varphi\varphi} - \bar{g}_{tt}g_{\varphi\varphi} \stackrel{!}{=} 0 \quad \text{with} \quad \bar{g} = g(r = r_0, \vartheta = \pi/2) \quad \text{and} \tag{5.1}$$

$$g_{tt} = -\left(1 - \frac{2M}{r}\right)\beta, \quad g_{t\varphi} = 0, \quad g_{\varphi\varphi} = \frac{r^2 \sin^2 \vartheta}{\beta} \tag{5.2}$$

This equation cannot be solved analytically because of the exponential r-dependence in β. The numerical solution, for different values of q, can be seen in figure 5.1.

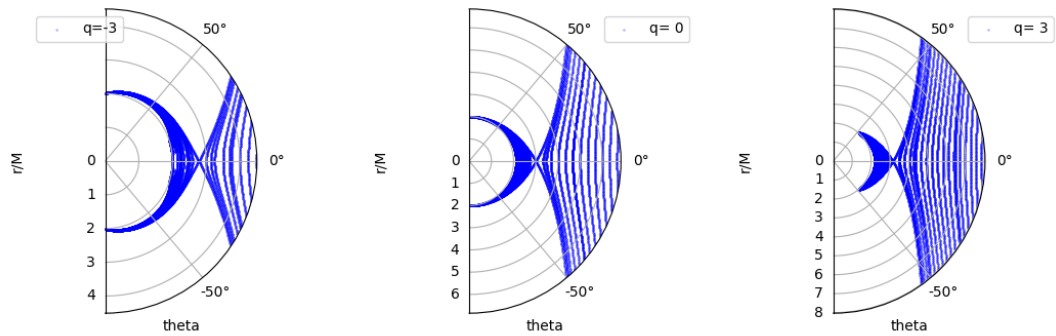
FIGURE 5.1: Equipotential surfaces of the von-Zeipel cylinders for 3 different values of the quadrupole parameter q. Left: $q = -3$; mid: $q = 0$, Schwarzschild limit; right: $q = 3$.

The blue lines indicate the equipotential surface for a fixed value of r_0. For increasing distance to the central object, the equipotential lines become increasingly less curved.

There are crossing surfaces for every value of q; for the Schwarzschild limit, the surface is found at $r_0 = 3M$. For negative values of q, the position of the crossing surfaces decreases; for positive values of q, the position of the crossing surface is larger than $r = 3M$.

5.2 Effective potential

In this section, geometrically thick tori are computed for compact objects, described by the Erez-Rosen Metric. For the calculation, the contravariant metric elements are needed (see section 2.3.3):

$$g^{tt} = -\frac{r}{(r-2M)}\frac{1}{\beta'}, \ \ g^{t\varphi} = 0, \ \ g^{\varphi\varphi} = \frac{\beta}{r^2\sin^2\vartheta} \tag{5.3}$$

Again, the $g^{t\varphi}$ component of the metric vanishes as the spacetime is static.
The four-velocity (cf. Eq. (2.36)) can be calculated as

$$u_t^{-2} = \frac{r^3\sin^2\vartheta - l^2(r-2M)\beta^2}{r^2(r-2M)\sin^2\vartheta\cdot\beta} \tag{5.4}$$

Regarding this, the effective potential for the geometrically thick tori in Erez-Rosen spacetime is given by (see Eq. (2.35)):

$$\mathcal{W} = \frac{1}{2}\ln\left[\frac{r^2(r-2M)\sin^2\vartheta\cdot\beta}{r^3\sin^2\vartheta - l^2(r-2M)\beta^2}\right] \tag{5.5}$$

This reduces to the known expression in Schwarzschild spacetime (Eq. (3.7)) for $q = 0 \rightarrow \beta = 1$.

To study the behavior of the tori in Erez-Rosen spacetime, the effective potential in Eq. (5.5) is observed in the equatorial plane $\vartheta = \pi/2$. The graph for 3 different quadrupole moments is depicted in figure 5.2.
 Similar to the Schwarzschild case, the outermost closed equipotential surface of the torus is indicated by the blue dashed line. The intersection of this line and the effective potential marks the location of the cusp and the outer edge of the torus, the green shaded area indicates the Roche limit of the respective effective potential.

In order to better grasp the geometry of the tori, the dependency of the effective potential on the angle ϑ is computed. As there is a exponential r-dependence in β_0, this is only computed numerically; the course of the effective potential for different values of q is shown in figure 5.3.
 The distinct colors represent the polar dependency of the effective potential for 3 different values of q, including the Schwarzschild limit in $q = 0$.

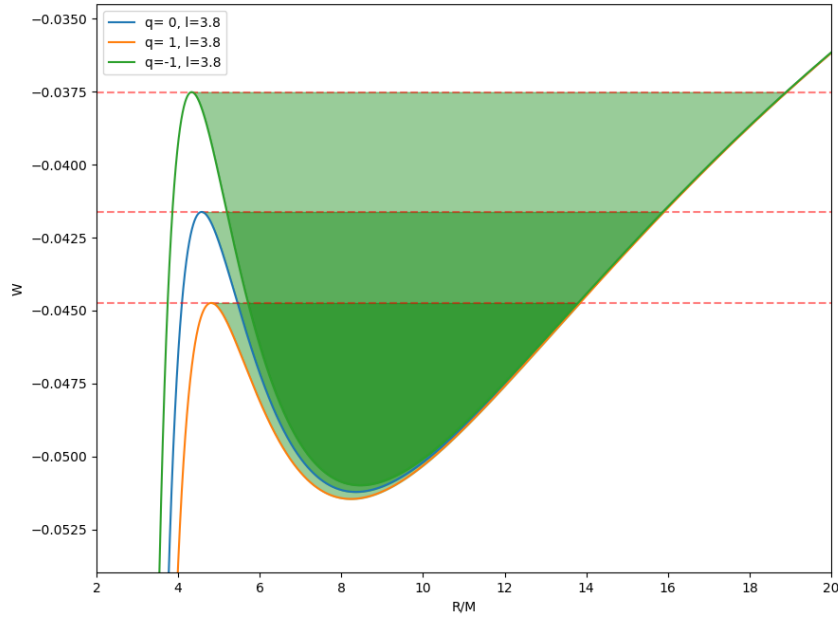The influence of the quadrupole parameter on the effective potential is be discussed in detail in section 5.4.

FIGURE 5.2: Representative behavior of the effective potential, in dependency of r/M, in the equatorial plane for 3 different values of the quadrupole $q = \pm 1$ and $q = 0$, the latter representing the Schwarzschild limit. The green filled area indicated the maximum region that can be filled by the fluid.
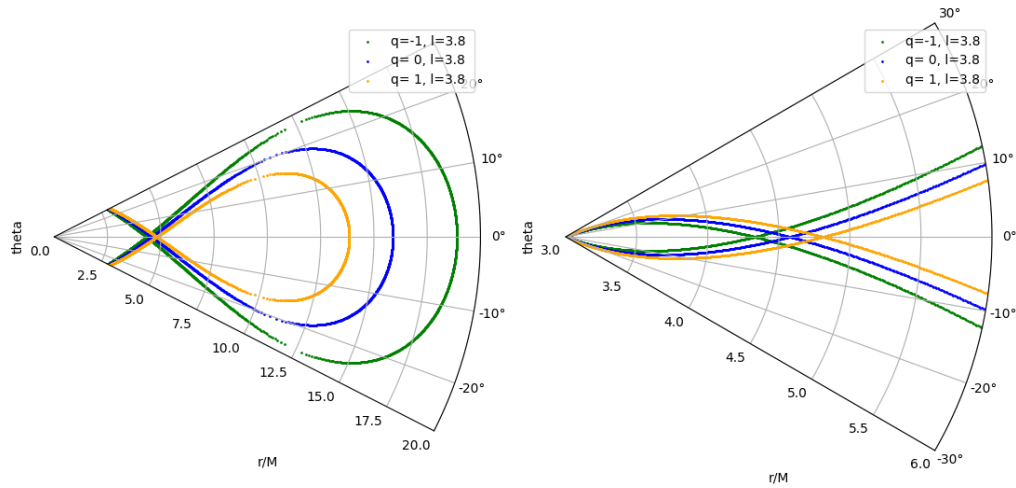

FIGURE 5.3: Polar dependency of the effective potential on the radius for 3 different values of the quadrupole parameter; green: $q = 1$, blue: $q = 0$ (Schwarzschild limit), orange: $q = -1$. Left: Polar dependency at bigger distance, showing the full geometric properties; Right: zoom on the position of the cusp for the three values of q.

5.3   Limits to the specific angular momentum

In this section, the limits to the specific angular momentum in Erez-Rosen spacetime, depending on the quadrupole parameter q, are discussed. In this regard, the Keplerian specific angular momentum (KSAM) is of importance, and is consequently discussed first.

5.3.1   Keplerian specific angular momentum

In the following, the Keplerian specific angular momentum for tori in Erez-Rosen spacetime is calculated. The calculation follows the general approach outlined in section 2.5.
Thus, the Keplerian angular velocity is computed, following Eq. (2.37). The covariant metric components in the equatorial plane can be written as[1]

$$g_{tt} = -\left(1 - \frac{2M}{r}\right)\beta_0, \quad g_{t\varphi} = 0, \quad g_{\varphi\varphi} = \frac{r^2}{\beta_0} \tag{5.6}$$

where $g_{t\varphi}$ vanishes as the spacetime is static.

With $\partial_r \beta_0 = q\left(1 - \frac{2M}{r}\right)u(r,q)\beta_0$ (see Eq. (2.26)), the Keplerian angular velocity can be expressed as:

$$\Omega_K^2 \nabla_\mu g_{\varphi\varphi} = -\nabla_\mu g_{tt}$$

$$\Leftrightarrow \ \Omega_K^2 \cdot \partial_r\left(\frac{r^2}{\beta_0}\right) = \partial_r\left[\left(1 - \frac{2M}{r}\right)\beta_0\right]$$

$$\Leftrightarrow \qquad \Omega_K^2 = \frac{\left[\frac{2M}{r^2} + q\left(1 - \frac{2M}{r}\right)u(r,q)\right]\beta_0^2}{2r - qu(r,q)r^2}$$

$$=: \frac{\kappa(r,q)}{2r - qu(r,q)r^2} \cdot \beta_0^2 \tag{5.7}$$

This expression reduces trivially to the Schwarzschild Keplerian angular momentum $\Omega_K^2 = \frac{M}{r^3}$, when taking into account $\beta_0(q=0) = 1$ and $\kappa(r,0) = \frac{2M}{r^2}$.

Following Eq. (2.39), the Keplerian specific angular momentum can be calculated as

$$\Omega_K^2 = \left(\frac{g^{\varphi\varphi}}{g^{tt}}\right)^2 \cdot l_K^2$$

$$\Leftrightarrow \frac{\kappa(r,q)}{2r - qu(r,q)r^2} \cdot \beta_0^2 = \left(\frac{r^3}{r - 2M}\frac{1}{\beta_0}\right)^2 \cdot l_K^2$$

$$\Rightarrow \qquad l_K^2 = \frac{r^5}{(r - 2M)^2\beta_0^2} \cdot \frac{\kappa(r,q)}{2 - qu(r,q)r} \tag{5.8}$$

The Keplerian specific angular momentum is a cornerstone of the computation of the marginally stable- and marginally bound specific angular momentum.
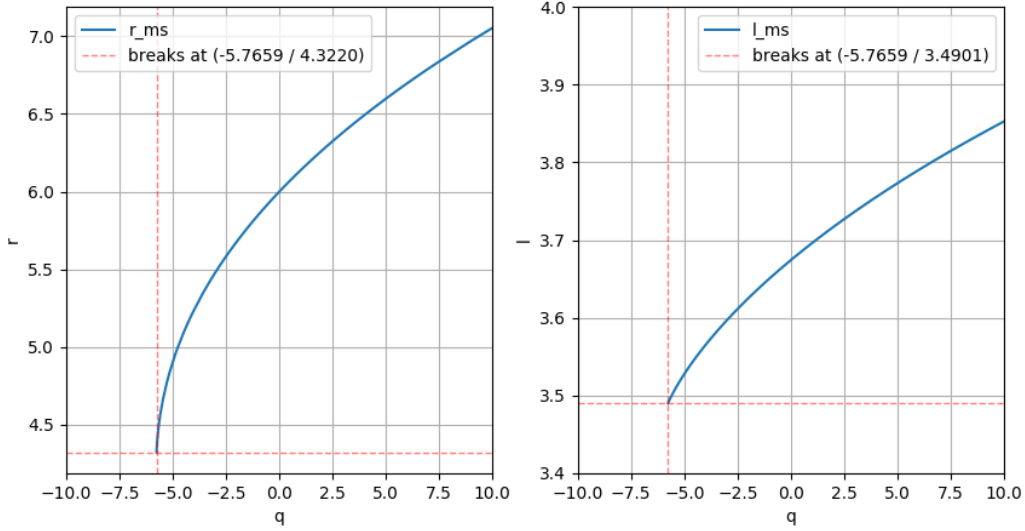
---

[1]For the definition of β_0, see Eq. (2.24).

FIGURE 5.4: Course of the marginally stable circular orbits and corresponding specific angular momentum, depending on the quadrupole parameter q. Left: marginally stable circular orbit; right: marginally stable specific angular momentum.

Schwarzschild limit $q = 0$

Considering $\beta_0(q = 0) = 1$ and $\kappa(r, 0) = \frac{2M}{r^2}$, the Keplerian specific angular momentum reduces to

$$l_K^2 = \frac{r^5}{(r - 2M)^2} \frac{\frac{2M}{r^2}}{2} = \frac{r^5}{(r - 2M)^2} \frac{M}{r^2} = \frac{Mr^3}{(r - 2M)^2}$$

which is the expression for the KSAM in Schwarzschild spacetime, see Eq. (3.10).

5.3.2 Marginally stable specific angular momentum

To determine the marginally stable circular orbit r_{MS}, and subsequently the marginally stable specific angular momentum l_{MS}, one needs to find the position of the minimum of l_K.
While the computation of the derivative in respective to r is feasible yet cumbersome, there is no exact analytic way to solve it for r, as there is an additional exponential r-dependence in β_0. In this regard, it is practicable to compute r_{MS} and l_{MS} numerically. The dependence of both values on the quadrupole parameter q can be seen in figure 5.4.

Numerical analysis shows that the marginally stable radius and angular momentum reduce to their respective values in Schwarzschild spacetime ($r_{\text{MS}} = 6M$ and $l_{\text{MS}} \approx 3.67M$)[2] for $q = 0$. The marginally stable radius (and consequently the marginally stable specific angular momentum) increases monotonically with q. There is a smallest value of r_{MS} at $(q, r) \approx (-5.77/4.32)$, which corresponds to a minimal l_{MS} at $(q, l) \approx (-5.77/3.49)$.

---

[2]For the exact values, see Eq. (3.11) and (3.12).

5.3.3   Marginally bound specific angular momentum

In this section, the marginally bound circular orbit and -specific angular momentum are calculated.

The calculation follows the procedure that is introduced in more detail in section 2.5. Regarding this, the minimum of the geodetic effective potential (see Eq. (2.23)) needs to be observed, which results in a condition for the angular momentum of a test particle orbiting the central object.

The detailed calculation can be seen in the appendix, section A.2.1, which results in the following expression for the angular momentum:

$$V_{\text{eff}} = \left(1 - \frac{2M}{r}\right)\beta_0 \left[\beta_0 \frac{l^2}{r^2} + 1\right] \tag{5.9}$$

$$l^2 = \frac{\kappa(r,q)r^4}{2\beta_0}\frac{1}{r - M - \kappa(r,q)r^2} \quad \text{with} \quad \kappa(r,q) = \left[\frac{2M}{r^2} + q\left(1 - \frac{2M}{r}\right)u(r,q)\right] \tag{5.10}$$

Schwarzschild limit $q = 0$

Considering $\kappa(r,0) = \frac{2M}{r^2}$ and $\beta_0(q = 0) = 1$, the expression above reduces to

$$l^2 = \frac{\frac{2M}{r^2}r^4}{2} \cdot \frac{1}{r - M - 2M} = \frac{Mr^2}{r - 3M}, \tag{5.11}$$

which results indeed in the expression found in Schwarzschild spacetime (cf. Eq. (3.13)).

The marginally bound orbit can now be found by inserting the expression for the angular momentum back into the effective potential in Eq. (5.9) to calculate V_{extr} and setting it to 1; solving this equation for r gives the marginally bound circular orbit r_{MB}.

Similar to the calculation of the marginally stable circular orbit, there is no exact analytical expression for r_{MB}; therefore, the following analysis is restricted to numerical computations. With the numerically obtained marginally bound circular orbit, the marginally bound angular momentum l_{MB} can be computed as the Keplerian specific angular momentum at r_{MB}.

Both r_{MB} and l_{MB}, depending on the quadrupole parameter q, are depicted in figure 5.5.

The marginally bound orbit, and subsequently the marginally bound angular momentum, is monotonically increasing with the quadrupole parameter. There is a minimal value of r_{MB} at $(q, r) \approx (-3.93/3)$ and a corresponding minimum of l_{MB} at $(q, r) \approx (-3.93/3.82)$.

However, the marginally bound circular orbit drops below the photon circular orbit (see Eq. (2.28) and figure 2.1) when approaching $q \approx -3.93$. This suggests that there is another limiting factor regarding the specific angular momentum.

There is a lower boundary to any timelike circular orbit, derived from the denominator in Eq. (5.10) and given by the condition[3]:

$$r - M - \kappa(r,q)r^2 > 0, \tag{5.12}$$

where the limiting case $r - M - \kappa(r,q)r^2 = 0$ marks the position of the photon circle r_c. The third condition for the specific angular momentum is consequently received by calculating $l_K(r_c)$.
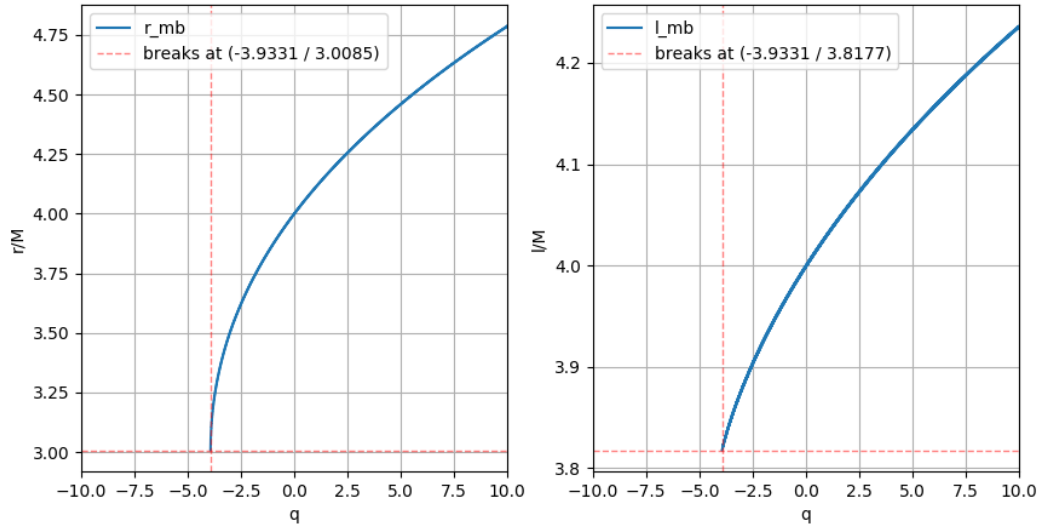
---

[3]Again, also see Eq. (2.28).

FIGURE 5.5: Course of the marginally bound circular orbit and corresponding specific angular momentum as a function of the quadrupole parameter q. Left: marginally bound circular orbit; right: marginally bound specific angular momentum.

Summary

In this section, the marginally stable and marginally bound angular momenta were computed, as well as the Keplerian specific angular momentum, evaluated at the $r = r_c$.

The dependence of all 3 limits of the specific angular momentum on the quadrupole parameter are shown in figure 5.6. There are closed equipotential surfaces only for pairs of values (q, l) enclosed by these 3 curves, indicated by the red shaded area.

It is essential to notice that while there are 2 photon circles for $1 < q \lesssim 2.253$, the Keplerian specific angular momentum increases rapidly for $r \to 2M$, and thus l_{MB} dictates the upper limit of the specific angular momentum in this region.

5.4 Influence of the quadrupole parameter on the behavior of the tori

In this section, the influence of the quadrupole parameter of the behavior and geometry of the tori is discussed. In particular, the geometrical properties can be seen in figure 5.2 and 5.3.

The shape of the effective potential is similar for different values of q, as it possesses one local maximum and -minimum. The position of the cusp moves to increasing values of r/M for greater values of q. Contrary, the value of the effective potential at the cusp increases for decreasing values of q. This leads to a torus that extends farther into space. For high values of r/M, the influence of the quadrupole parameter becomes negligible, as the effective potentials for different values of q draw close to each other.

When looking at the polar dependency of the effective potential (see figure 5.3), the position of the cusp moves only slightly, decreasing for negative values of q. On the contrary, the tori with a negative quadrupole parameter extend farther into space, as well as extending more above and below the equatorial plane.
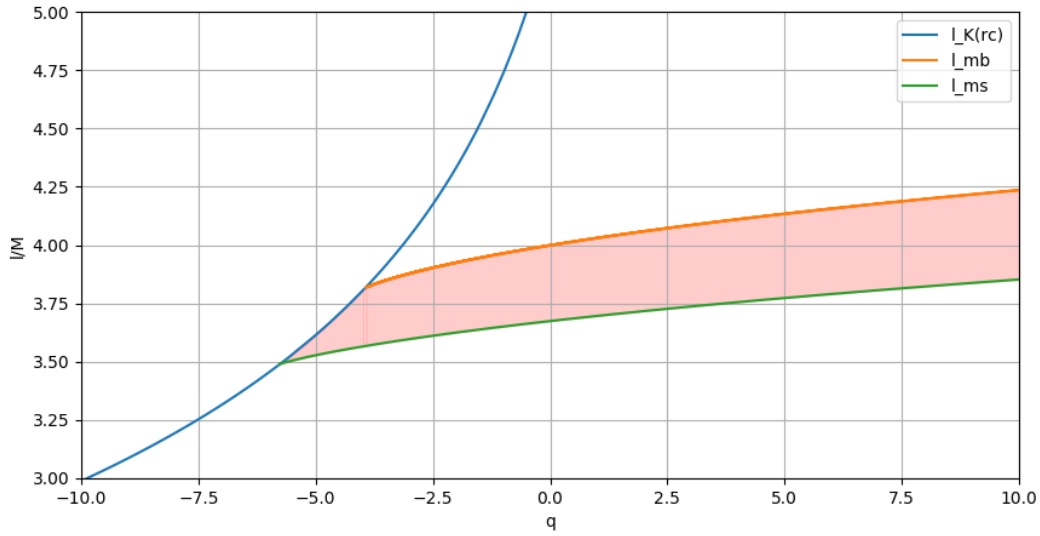
FIGURE 5.6: Plot of the marginally bound- and marginally stable specific angular momentum, as well as the Keplerian specific angular momentum, evaluated at the photon circle. The red shaded area indicates values of q and l that result in closed equipotential surfaces for geometrically thick tori in Erez-Rosen spacetime.
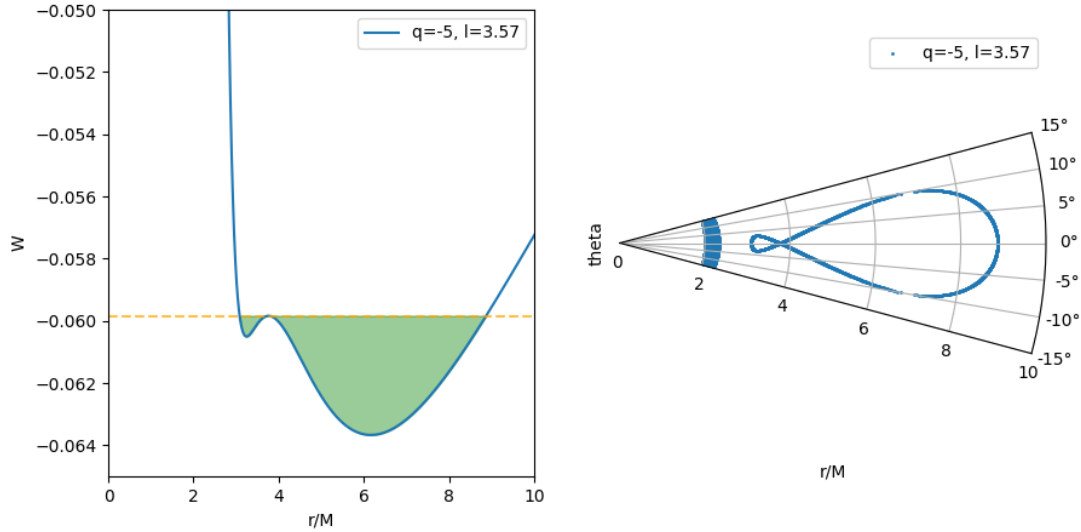

FIGURE 5.7: Representation of the effective potential with its quadrupole parameter lying in the region $-5.77 \lesssim q \lesssim -3.93$. Left: effective potential in the equatorial plane, the green shaded area indicating its Roche limit; right: polar dependency of the effective potential.

Geometrically thick tori in the region $-5.77 \lesssim q \lesssim -3.93$

In contrast to the Schwarzschild case, there is a region that is not bound by the marginally bound specific angular momentum, but rather by the Keplerian specific angular momentum at the photon circle. The behavior of tori with configurations in this region is generally different from the Schwarzschild-like tori for $q \gtrsim -3.93$. The effective potential in the equatorial plane and the polar dependency at $q = -5$ is shown in figure 5.7.

For $r \to 2M$, the effective potential approaches positive infinity, instead of negative infinity for Schwarzschild-like configurations, as can be seen in figure 5.2. This generates the following effect; in addition to one local maximum, the effective potential shows two local minima, instead of one. The local maximum serves as a separator, dividing the torus into two different closed surfaces, the inner and outer torus. The distance between the two tori is dictated by the amount of mass of the torus; if the torus is filling its Roche limit, the distance becomes infinitesimally small. The inner torus can disappear if there is not enough matter, with the effective potential dropping below the first local minimum.
In principle, the torus can fill beyond its Roche limit; in this case, the inner edge of the torus drops below the critical radius, set by the condition in Eq. (5.12), and is thus prohibited.

Chapter 6

Comparison of the influence of the quadrupole on geometrically thick tori

In the last chapters, geometrically thick tori and the limits on their specific angular momentum were discussed. For tori in Erez-Rosen spacetime and the q-metric, the influence of the quadrupole parameter on the geometrical properties and general behavior were detailed.

In the following, the influence of the quadrupole moment on the geometrically thick tori is compared for these two spacetimes, particularly in regards to the Schwarzschild case of $q = 0$.

6.1 Influence of the quadrupole parameter on the geometrical properties of the effective potential

In this section, the influence of the quadrupole parameter on the effective potential in Erez-Rosen spacetime and the q-metric is discussed. In this regard, the polar dependency of the effective potential for the three different spacetimes is depicted in figure 6.1.
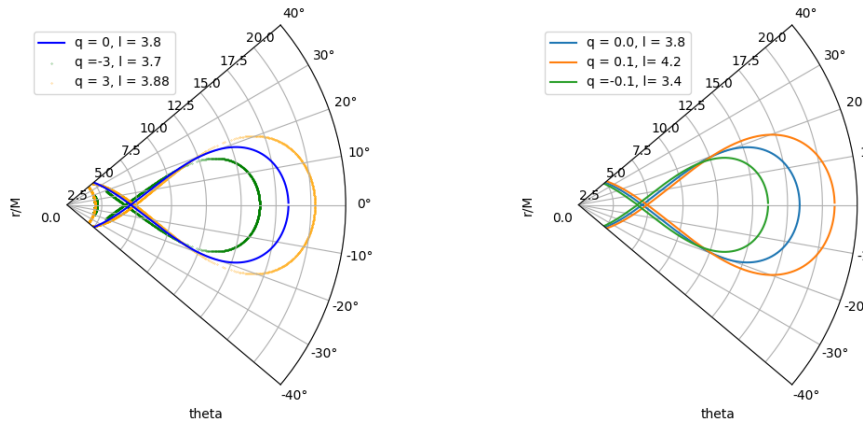

FIGURE 6.1: Influence of the quadrupole on the effective potential. Left: Polar dependency for tori in Erez-Rosen spacetime; right: polar dependency for tori orbiting a compact object, described by the q-metric. Green: tori with negative quadrupole parameter; blue: $q = 0$, Schwarzschild limit; orange: positive quadrupole parameter.

In general, the geometrical behavior of the effective potential does not change qualitatively significantly, possessing a cusp, which subdivides the torus into a closed surfaces and a surfaces that extends onto the compact object.

For both spacetimes, the cusp of the geometrically thick tori moves with non-vanishing quadrupole
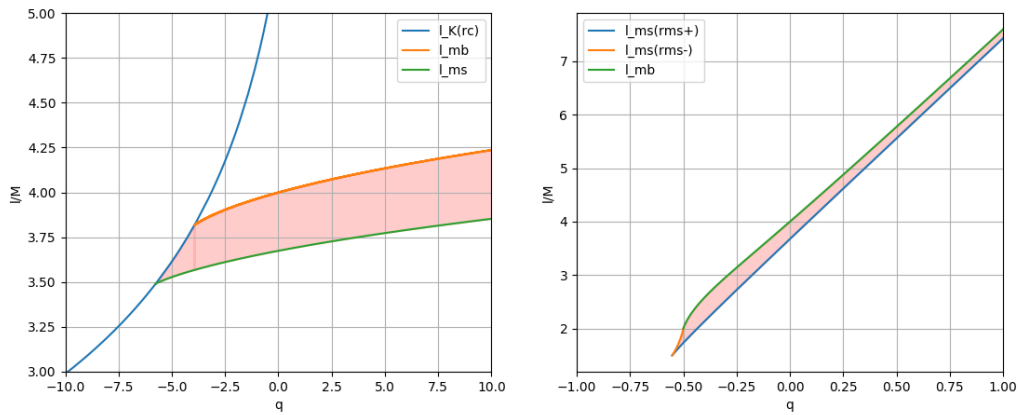
FIGURE 6.2: Limits of the specific angular momentum, depending on the quadrupole parameter. Left: limits of the angular momentum in Erez-Rosen spacetime; right: limits of the angular momentum for the q-metric.

moment. In particular, in comparison with the Schwarzschild case: for negative quadrupole parameter, the cusp moves to smaller r/M; for positive quadrupole parameter, the cusp moves to higher values of r/M.

While the quantitative values of the quadrupole parameter range and position of cusp differs between tori in Erez-Rosen spacetime and q-metric, this qualitative behavior is similar when comparing the influence of the quadrupole parameter on the cusp. Additionally, the tori with negative quadrupole parameter generally extends less far into space, while tori with positive quadrupole parameter extends farther into space, compared to the Schwarzschild limit.

This suggests that the change of the position of the cusp and extension into space are properties of tori in spacetime with non-vanishing quadrupole moment.

6.2　Influence of the quadrupole parameter on the limits of the specific angular momentum

In this section, the influence of the quadrupole parameter on the upper and lower limit of the angular momentum of the geometrically thick tori is discussed. Particularly, the marginally stable and marginally bound specific angular momentum, serving as the upper and lower limit respectively, are to be compared.

These limits are shown in figure 6.2. For both spacetimes, l_{MS} and l_{MB} show the same qualitative behavior; there is no upper bound on the marginally stable or marginally bound angular momentum, but a lower boundary for negative values of q. In both cases, the limits reduce to their Schwarzschild equivalents for $q = 0$.

The lower boundary of the marginally stable angular momentum lies at lower values of q than the lower boundary of l_{MB}. Thus, there is a region at negative q where the marginally bound angular momentum does not serve as the upper boundary of the specific angular momentum. For the q-metric, this region corresponds to the region where there are two marginally stable circular orbits; the Keplerian specific angular momentum at the negative and positive solution marks the upper and lower boundary, respectively.

For the Erez-Rosen spacetime, the upper boundary in this region corresponds the Keplerian specific angular momentum at the position of the photon circle.

Tori described by a quadrupole parameter in this interval show qualitatively different geometrical behavior, compared to the Schwarzschild limit. These will be discussed in the following
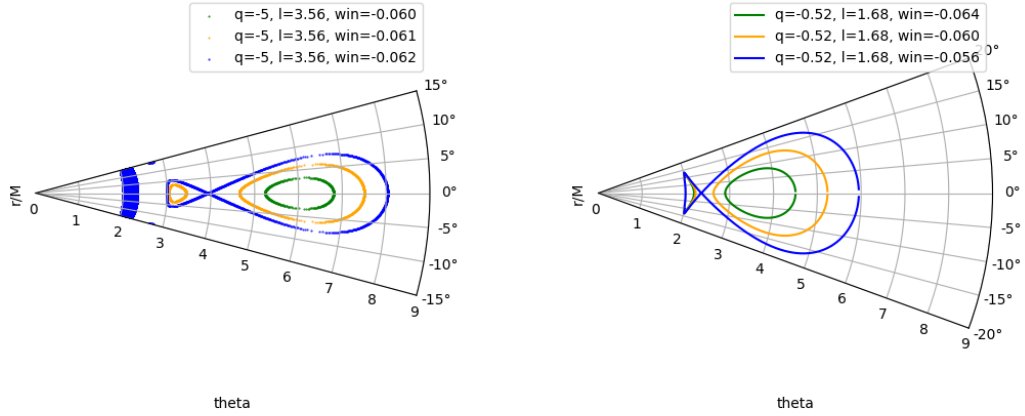
FIGURE 6.3: Polar dependency of the effective potential for quadrupole parameter, selected from the region when there is no marginally bound specific angular momentum. Left: Torus orbiting an compact object that is described by the q-metric; right: torus orbiting an compact object described by Erez-Rosen metric. The blue lines indicate the Roche lobe for the given (q, l); the orange and green colored lines indicate tori that are not filled to their Roche limit.

section.

The similarities of the upper and lower limits between the two examined spacetimes suggest that this behavior may be a property shared by geometrically thick tori orbiting compact objects with non-vanishing quadrupole moment.

6.3 Geometrically thick tori with quadrupole moment in the region without a marginally bound specific angular momentum

In this section, the behavior and properties of geometrically thick tori in the region of q without a marginally bound specific angular momentum are explored more closely. In particular, as both spacetimes posses such a region, tori in this region are compared between the two quadrupole spacetimes.
 The behavior of these tori can be seen in figure 6.3.
For both spacetimes, there exist two closed surfaces, splitting the original torus into an inner and outer torus. If the tori are not filled up to their Roche lobe, the inner and outer tori are spatially separated.
Qualitatively, the tori in the two spacetimes show similar behavior. However, the tori in the q-metric extend less far into space, but stretches out to higher angles ϑ, compared to the tori in Erez-Rosen spacetime. Additionally, while the tori in the q-metric extends very close to $r = 2M$, the inner edge of the inner torus in Erez-Rosen spacetime is significantly greater than $r = 2M$.

As both spacetimes possess a region of q where there is no marginally bound angular momentum, serving as a upper limit of the specific angular momentum, and tori in this region show deviating behavior to the Schwarzschild tori, splitting into two tori, it is reasonable to assume that this may be a property of geometrically thick tori orbiting compact objects with non-vanishing quadrupole moment.

Chapter 7

Conclusion

In the course of this thesis, geometrically thick tori orbiting compact object with quadrupole moment were studied. In particular, the limits of the specific angular momentum and the influence of the quadrupole moment on the behavior of the tori were examined in more detail.

Firstly, geometrically thick tori around a Schwarzschild black hole were discussed. They have a cusp indicated by a fluid filling its Roche lobe. True to their name, when looking at the polar dependency of the effective potential, these fluids form tori around the central object. The specific angular momentum of the tori is limited by the marginally stable - and marginally bound specific angular momentum, and was determined to be $3.67 \lesssim l/M < 4$.
The Schwarzschild tori were then used as a reference for discussing the limit of the quadrupole spacetimes with vanishing quadrupole moment.

After this, there was a discussion on geometrically thick tori orbiting a compact object that is described by the q-metric. Tori in the q-metric, the simplest exact solution of the vacuum field equations with quadrupole moment, show qualitatively similar behavior, when compared to tori in Schwarzschild spacetime. The position of the cusp moves for non-vanishing quadrupole moment, increasing for positive and decreasing for negative quadrupole parameter.
Furthermore, the limits on the specific angular momentum were calculated. For positive values of q, tori with quadrupole parameter in this region are qualitatively similar, compared to the Schwarzschild tori. For negative values of q, there exists a region $-0.553 \lesssim q < -0.5$ where there is no marginally bound specific angular momentum serving as the upper limit. However, there is a second marginally stable specific angular momentum, connecting smoothly to the marginally bound case at $q = -0.5$. Tori with a quadrupole parameter in this interval show a qualitatively different behavior compared to the Schwarzschild case; these tori have two closed surfaces, separating the initial torus into a inner and outer torus. The cusp separates the two tori, and the inner edge of the inner torus extends very close to $r = 2M$.

Afterwards, geometrically thick tori orbiting a compact object in Erez-Rosen spacetime were discussed. Tori in Erez-Rosen spacetime, the first exact solution to the field equations with multipole moments up to the quadrupole moment, show qualitatively similar behavior when compared to the Schwarzschild case as well. Again, the position of the cusp moves for non-vanishing quadrupole moment, increasing to a greater distance with increasing quadrupole parameter and decreasing to a lesser distance with decreasing quadrupole parameter.
Moreover, the limits of the specific angular momentum were computed. For positive quadrupole parameter, the tori behave in a similar way compared to the Schwarzschild tori, l_{MB} and l_{MS} serving as the upper and lower limit, respectively. For negative values of the quadrupole parameter, however, there is a region $-5.77 \lesssim q \lesssim -3.93$ where there is no marginally bound angular momentum anymore which would serve as the upper limit. It was shown that the upper limit can be calculated as the Keplerian specific angular momentum at the position of the photon circle. Tori with a quadrupole parameter in this parameter range show qualitatively

differing behavior to tori in Schwarzschild spacetime; the initial torus splits into two tori at the cusp, dividing it into an inner and outer torus.

Lastly, the influence of the quadrupole parameter on the behavior of the geometrically thick tori was compared for the two spacetimes.
In general, the geometrical properties of geometrically thick tori with quadrupole moment are similar to the Schwarzschild case; there are closed configurations with a pronounced cusp, indicated by the fluid filling its Roche lobe. Qualitatively, the change on the behavior of the tori, compared to the Schwarzschild case, is similar between the two spacetimes; for non-vanishing quadrupole parameter, the position of the cusp moves, depending on whether the quadrupole parameter is greater or smaller than 0.
The limits on the specific angular momentum are similar for both quadrupole spacetimes, the marginally stable and bound specific angular momentum have a lower bound for negative q, but no upper boundary. Additionally, both spacetime have a interval of the quadrupole parameter where there is no l_{MB} anymore which would serve as the upper limit. In this region, the torus splits into a inner and outer torus at the cusp, as the effective potential possesses a second local minimum for $r > 2M$.

The properties of geometrically thick tori orbiting a compact object with quadrupole moment are shared between the two spacetimes, which may indicate that the movement of the cusp, as well as the region without a marginally bound angular momentum and the associated division of the torus into two, is a property of tori orbiting any quadrupolar object.

Appendix A

Computations

A.1 Computations in the Q-Metric

A.1.1 Marginally stable circular orbit

$$\partial_r l_K = \partial_r \frac{r\sqrt{M(q+1)}}{\alpha^{1+q}\sqrt{r-Mq\alpha^{-1}}} = 0 \qquad \text{(A.1)}$$

$$\Leftrightarrow \frac{r\sqrt{M(q+1)}\left(-\frac{1}{2}-\frac{M^2q}{\alpha^2r^2}\right)}{\alpha^{1+q}\sqrt{r-Mq\alpha^{-1}}} + \frac{\sqrt{M(q+1)}}{\alpha^{1+q}\sqrt{r-Mq\alpha^{-1}}} - \frac{2M(q+1)\sqrt{M(q+1)}}{\alpha^{q+1}\alpha r\sqrt{r-Mq\alpha^{-1}}} = 0 \qquad \text{(A.2)}$$

Note: As seen in equation A.2, this equation is imaginary for all values of r for $q < -1$. In fact, the KSAM is strictly 0 everywhere for $q = -1$.
Thus, the discussion is limited to $q > -1$ (and $r \neq 2M$, of course). Dividing equation A.2 by $\sqrt{M(q+1)}$ and multiplying with $\alpha^{1+q}\sqrt{r-Mq\alpha^{-1}}$ yields[1]:

$$\Leftrightarrow \frac{r\left(-\frac{1}{2}-\frac{M^2q}{\alpha^2r^2}\right)}{r-Mq\alpha^{-1}} + 1 - \frac{2M(q+1)}{\alpha r} = 0 \qquad \text{(A.3)}$$

$$\Leftrightarrow r^2\alpha\left(-\frac{1}{2}-\frac{M^2q}{\alpha^2r^2}\right) + \alpha r(r-Mq\alpha^{-1}) - 2M(q+1)(r-Mq\alpha^{-1}) = 0 \qquad \text{(A.4)}$$

$$\Leftrightarrow r\alpha\left(-\frac{1}{2}-\frac{M^2q}{\alpha^2r^2}\right) + \alpha r\left(1-\frac{Mq}{r-2M}\right) - 2M(q+1)\left(1-\frac{Mq}{r-2M}\right) = 0 \qquad \text{(A.5)}$$

$$\Leftrightarrow r\alpha\left(\frac{1}{2}-\frac{M^2q}{(r-2M)^2}-\frac{Mq}{r-2M}\right) - 2M(q+1)\left(1-\frac{Mq}{r-2M}\right) = 0 \qquad \text{(A.6)}$$

$$\Leftrightarrow r-2M-\frac{M^2q}{r-2M}-Mq+2M(q+1)\left(1-\frac{Mq}{r-2M}\right) = 0 \qquad \text{(A.7)}$$

$$\Leftrightarrow r^2 - (8+6q)r + (-q^2+2q+8) = 0 \qquad \text{(A.8)}$$

$$\Leftrightarrow r_{\text{MS}}^{\pm} = M\left(4+3q\pm\sqrt{5q^2+10q+4}\right) \qquad \text{(A.9)}$$

---

[1]I also used that $\alpha^{-1} = \frac{r}{r-2M}$ and $r\cdot\alpha = r-2M$

A.2   Computations in Erez-Rosen spacetime

A.2.1   Computing the derivative of the effective potential

With

$$\kappa(r) = \left[\frac{2M}{r^2} + q\left(1 - \frac{2M}{r}\right)u(r)\right] \tag{A.10}$$

One can find:

$$\partial_r V_{\text{eff}} = \kappa(r)\beta\left[1 + \frac{\beta l^2}{r^2}\right] \tag{A.11}$$

$$+ \left(1 - \frac{2M}{r}\right)\beta\left[qu(r)\frac{\beta l^2}{r^2} - 2\frac{\beta l^2}{r^3}\right] \overset{!}{=} 0 \tag{A.12}$$

$$\Leftrightarrow 0 = \kappa(r)\left[1 + \frac{\beta l^2}{r^2}\right] \tag{A.13}$$

$$+ \frac{l^2}{r^2}\beta\left[q\left(1 - \frac{2M}{r}\right)u(r) - \frac{2(r - 2M)}{r^2}\right] \tag{A.14}$$

$$\Leftrightarrow 0 = \kappa(r)\left[1 + \frac{\beta l^2}{r^2}\right] \tag{A.15}$$

$$+ \frac{l^2}{r^2}\beta\left[\underbrace{q\left(1 - \frac{2M}{r}\right)u(r) + \frac{2M}{r^2}}_{=\kappa(r)} - \frac{2(r - M)}{r^2}\right] \tag{A.16}$$

$$\Leftrightarrow 0 = \kappa(r) + \frac{l^2}{r^2}\beta\left[\kappa(r) + \kappa(r) - 2\frac{r - M}{r^2}\right] \tag{A.17}$$

$$\Leftrightarrow -\kappa(r) = l^2\frac{2\beta}{r^4}\left[\kappa(r)r^2 - r + M\right] \tag{A.18}$$

$$\Leftrightarrow l^2 = \frac{\kappa(r)r^4}{2\beta}\frac{1}{r - M - \kappa(r)r^2} \quad \square \tag{A.19}$$

Bibliography

[1] R. M. Wald, *General relativity*. Chicago, IL: Chicago Univ. Press, 1984.

[2] H. Weyl, *Raum — Zeit — Materie*, vol. 5. Springer (Berlin), 1923.

[3] M. M. G. Ricci and T. Levi Civita, "Méthodes de calcul différentiel absolu et leurs applications," Jan. 1970.

[4] A. Einstein, "Die Grundlage der allgemeinen Relativitätstheorie," *Annalen der Physik*, vol. 354, pp. 769–822, Jan. 1916.

[5] B. Coll, J. J. Ferrando, and J. A. Sáez, "Relativistic perfect fluids in local thermal equilibrium," *Gen. Rel. Grav.*, vol. 49, no. 5, p. 66, 2017.

[6] J. Frauendiener, "A note on the relativistic euler equations," *Classical and Quantum Gravity*, vol. 20, pp. L193–L196, 07 2003.

[7] J. B. Griffiths and J. Podolský, *Exact space-times in Einstein's General Relativity*. Cambridge Monographs on Mathematical Physics, Cambridge University Press, 2009.

[8] K. Schwarzschild, "Über das Gravitationsfeld eines Massenpunktes nach der Einsteinschen Theorie," *Sitzungsberichte der Königlich Preußischen Akademie der Wissenschaften (Berlin)*, pp. 189–196, Jan. 1916.

[9] J. M. Heinzle and R. Steinbauer, "Remarks on the distributional schwarzschild geometry," *Journal of Mathematical Physics*, vol. 43, p. 1493–1508, Mar 2002.

[10] H. Lü and H.-D. Lyu, "Schwarzschild black holes have the largest size," *Phys. Rev. D*, vol. 101, p. 044059, Feb 2020.

[11] H. Weyl, "Zur Gravitationstheorie," *Annalen der Physik*, vol. 359, no. 18, pp. 117–145, 1917.

[12] H. Quevedo, "Mass Quadrupole as a Source of Naked Singularities," *Int. J. Mod. Phys.*, vol. D20, pp. 1779–1787, 2011.

[13] K. Boshkayev, E. Gasperin, A. Gutierrez-Pineres, H. Quevedo, and S. Toktarbay, "Motion of test particles in the field of a naked singularity," *Physical Review D*, vol. 93, 01 2016.

[14] G. Erez and N. Rosen, "The gravitational field of a particle possessing a multipole moment," *Bull. Research Council Israel*, vol. Vol: Sect. F.8, 9 1959.

[15] J. H. Young and C. A. Coulter, "Exact metric for a nonrotating mass with a quadrupole moment," *Phys. Rev.*, vol. 184, pp. 1313–1315, Aug 1969.

[16] D. Bini, M. Crosta, F. de Felice, A. Geralico, and A. Vecchiato, "The erez–rosen metric and the role of the quadrupole on light propagation," *Classical and Quantum Gravity*, vol. 30, p. 045009, jan 2013.

[17] E. Gourgoulhon, "An Introduction to relativistic hydrodynamics," *EAS Publ. Ser.*, vol. 21, pp. 43–79, 2006.

[18] L. Rezzolla and O. Zanotti, *Relativistic Hydrodynamics*. Oxford University Press, 2013.

[19] S. Chakrabarti, "Von Zeipel surfaces. II - A catalogue," *Monthly Notices of the Royal Astronomical Society*, vol. 250, pp. 7–13, 04 1991.

[20] D. Pugliese, G. Montani, and M. G. Bernardini, "On the Polish doughnut accretion disk via the effective potential approach," *Mon. Not. Roy. Astron. Soc.*, vol. 428, no. 2, pp. 952–982, 2013.

[21] Q. Lei, M. A. Abramowicz, P. C. Fragile, J. Horak, M. Machida, and O. Straub, "The Polish doughnuts revisited I. The angular momentum distribution and equipressure surfaces," *Astron. Astrophys.*, vol. 498, pp. 471–477, 2009.

[22] P. Becker, S. Das, and T. Le, "Diffusive particle acceleration in shocked, viscous accretion disks: Green's function energy distribution," *The Astrophysical Journal*, vol. 743, 01 2012.